Understanding Fe$_3$O$_4$ nanorod magnetism for biomedical applications

by

Rachel Alexandra Nickel

A thesis submitted to

The Faculty of Graduate Studies of

The University of Manitoba

in partial fulfillment of the requirements

of the degree of

Master of Science

Department of Physics and Astronomy

The University of Manitoba

Winnipeg, Manitoba, Canada

June 2018

Thesis advisor   Author

Dr. Johan van Lierop   **Rachel Alexandra Nickel**

Understanding Fe$_3$O$_4$ nanorod magnetism for biomedical applications

Abstract

Iron oxide nanoparticles have been extensively studied for a variety of applications; however, to optimize a system for a particular use requires a complete understanding of the underlying physics. Seemingly minor changes to size and shape can significantly affect a system's behaviour. In this work, we show how spherical iron oxide nanoparticles can be used to remove MRSA biofilms, with results that suggest anisotropic nanoparticles could be advantageous.

As a result, we have synthesized magnetite (Fe$_3$O$_4$) nanorods. By using a variety of techniques, such as x-ray diffraction, Mössbauer spectroscopy, XAS/XMDC and magnetometry, we have characterized this system. We observe a modified Verwey transition, where the low temperature monoclinic phase reveals a high degree of strain. By tracking the Fe$_3$O$_4$ nanorods' structure as a function of temperature, a multistep transition is observed with both transition temperatures elevated from the bulk Verwey temperature of $\sim$120 K. This suggests that the Verwey temperature could be controlled by manipulating the intrinsic strain. Of perhaps greater interest for biological applications is the response of the nanoparticles to a magnetic field. Much of the work thus far for applications such as hyperthermia treatments have

been focused on nanoparticles with domains that reverse via coherent rotation; however, our Fe_3O_4 nanorod domains reverse via curling. This effect is observed in the dependence of the intrinsic loss power on applied magnetic field and frequency. The measured heating efficiency of these Fe_3O_4 nanorods makes them excellent candidates for biomedical applications.

Contents

List of Figures

List of Tables

Acknowledgments

Firstly, I would like to thank my supervisor, Dr. Johan van Lierop, for his continued support throughout this process. His involvement has allowed me to grow and develop as a researcher. Without his encouragement, this work would not have been possible. I would also like to thank Dr. Song Liu, for his assistance with bacterial applications. His perseverance and helpful discussions have allowed this project to grow.

I would like to thank Jie Li for her invaluable assistance with the biofilm studies, and Katryna Fast for the nanorod hyperthermia measurements. Without you, this work would by missing key pieces. I would also like to thank all of the members of the Nanomagnetism Research Group for all of the assistance, helpful discussions and friendship you have provided. Special thanks to Peiqing Wang for his assistance with lab equipment and liquid helium. Additionally, I would like to thank the Physics and Astronomy office staff: Robyn Beaulieu, Susan Beshta, and Aymsley Bishop-Mahon for the support they provide to all students within the Department.

Finally, I would like to thank my family who have supported me throughout my studies.

Experimental Acknowledgments

I would like to thank Dr. Palash Manna for his assistance in nanoparticle synthesis and low temperature x-ray diffraction. While I have synthesized all of the samples within this work, he was key to the success of these samples. His trouble-shooting was critical to the acquisition of the low temperature diffraction measurements. I would like to thank Dr. Abdul Khan, for his assistance in acquiring TEM images of the initial nanoparticle samples, as well as training me on the instrument. I would especially like to thank Jie Li, for the many hours spent preparing, performing, and analyzing biofilm experiments. Many thanks to John Freeland and David Keavney at the APS for their technical support in XAS/XMCD measurements, and Johan van Lierop for assistance with XAS simulations. Finally, I would like to thank Katryna Fast for the hyperthermia measurements of the nanorod samples.

For my grandfather.

Chapter 1

Introduction

Magnetic nanoparticles are complex systems whose properties are determined by surface disorder and finite size effects.[1] Their unique characteristics make nanoparticles ideal for many applications such as recording media,[2] water treatment,[3] and a variety of biomedical applications.[4]

Iron oxides are of particular interest as the elements are naturally abundant and and readily synthesized as nanoparticles. There are multiple polymorphs of iron oxide, each with its own unique magnetism. Magnetite (Fe_3O_4) and maghemite (γ-Fe_2O_3) are both soft ferrimagnetic materials in the bulk. Due to their significant magnetic response and low toxicity, these phases are ideal for biomedical applications. Upon heating above 400°C, magnetite and maghemite will transform to different polymorphs.[5] Nanoparticles may transform to β-Fe_2O_3 and ϵ-Fe_2O_3 —metastable phases that only exist in the nanoscale.[6] Both of these phases have a high coercivity, making them possible candidates for recording media and rare earth-free permanent magnets. If any of these iron oxide phases is heated further to >1000°C, it will

transform to hematite (α-Fe$_2$O$_3$). α-Fe$_2$O$_3$ is the most thermodynamically stable iron oxide polymorph and is a canted antiferromagnetic. These nanoparticles have been used for a variety of applications, such as lithium ion batteries, gas sensors,[7] and solar cells.[8]

In this work, Fe$_3$O$_4$ nanoparticles for biomedical applications will be explored. Magnetite nanoparticles are ideal for many applications because they are easily synthesized and highly modifiable. Based on their low toxicity,[9] Fe$_3$O$_4$ nanoparticles have been studied for biomedical applications such as drug delivery,[10] imaging contrast,[11] and hyperthermia treatments.[12] Because the size, shape and surface properties of these nanoparticles can all be modified, there is a vast phase space to be explored. In particular, shape plays a significant role on the magnetism: Aspherical nanoparticles have been shown to be advantageous to drug delivery[13] and hyperthermia applications.[14][15]

1.1   Bulk Magnetism

In general, bulk magnetism arises as a result of the spontaneous alignment of magnetic moments due to their interactions. As shown in Figure 1.1, there are three types of magnetic ordering. In ferromagnetic materials, all magnetic moments are aligned below the Curie temperature (T$_C$). Antiferromagnetic materials are characterized by an antiparallel coupling where the magnetic moments compensate for each other within a unit cell. As a result, the net magnetization in an antiferromagnetic material is zero below the Néel temperature (T$_N$). When the antiparallel moments do not fully compensate for each other, the material is ferrimagnetic. Above the critical temper-
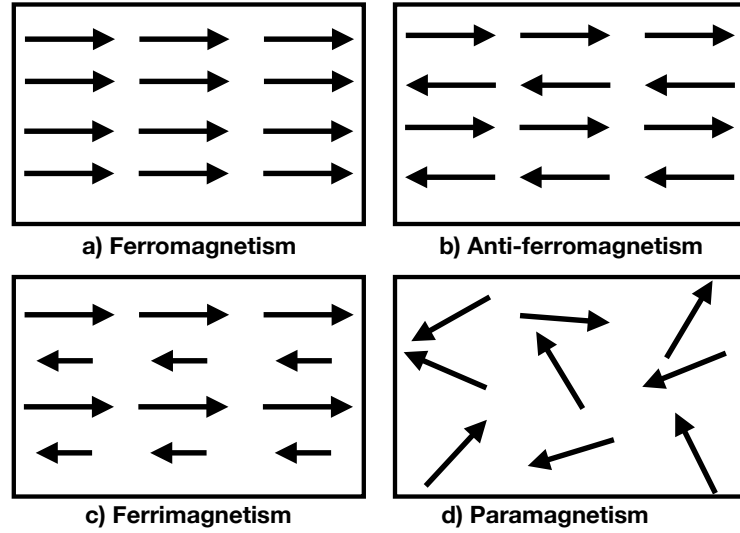
Figure 1.1: Schematic of the magnetic moment configurations for different types of magnetic materials.

ature (either T_C or T_N), thermal variations destroy the spontaneous magnetization and a disordered system with no net magnetic moment is obtained. Such a state is referred to as paramagnetic.

The interactions between ions responsible for the magnetic ordering are exchange based. This is a quantum mechanical effect resulting from Coulomb repulsion between electrons and the Pauli exclusion principle. Because the Pauli exclusion principle forbids two electrons from having the same quantum state, the parallel and antiparallel spin alignments result in different energies. The interaction between the spins of two atoms ($\vec{S}_a$ and $\vec{S}_b$) can be described by the Hamiltonion

$$\mathcal{H} = -2J\vec{S}_a \cdot \vec{S}_b \tag{1.1}$$

where J is the exchange integral, which describes the exchange configuration and
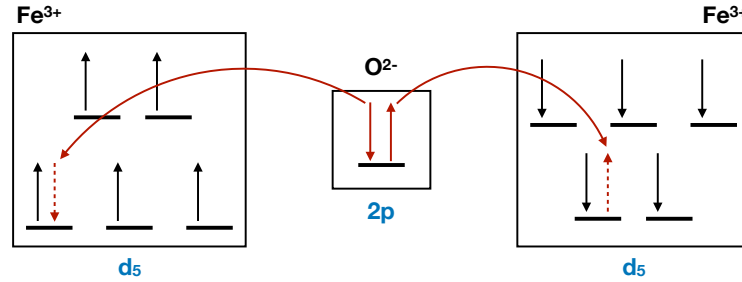
Figure 1.2: Schematic of the antiferromagnetic superexchange interaction between two Fe^{3+} ions mediated by O^{2-}.

strength. $J > 0$ describes a parallel spin alignment, while $J < 0$ describes an antiparallel spin alignment. When extrapolated over a material, the Hamiltonion

$$\mathcal{H} = -\sum_{a \neg b} J \vec{S}_a \cdot \vec{S}_b \tag{1.2}$$

describes the direct exchange interactions. However, there are other indirect exchange interactions that play a significant role in materials such as superexchange.

In transition metal oxides there is minimal overlap between the $3d$ metal orbitals. However, the overlap between the $3d$ orbitals with oxygen $2p$ orbitals enables an interaction between transition metal ions known as superexchange. Superexchange is the strong (typically anitiferromagnetic) coupling between two cations mediated by a non-magnetic anion. Here, the sign of the exchange integral (J) is determined by Pauli exclusion principle and Hund's rules. The Goodenough-Kanamori rules provide an empirical description of superexchange.[16][17] The antiferromagnetic superexchange interaction between two Fe^{3+} ions is shown in Figure 1.2.

When exposed to an external magnetic field, the tendency of the net magnetization ($\vec{M}$) to lie in a particular direction is represented by the magnetic anisotropy

(K). The overall anisotropy of a system is made up of multiple factors, including magnetocrystalline, shape and strain anisotropy. Magnetocrystalline anisotropy (K_u) is intrinsic to the material. It is the result of the spin-orbit interaction which couples the spin direction to the crystal lattice and leads to the formation of magnetic "easy" and "hard" axes. The energy (E_A) required to rotate the magnetization from an "easy" crystalline direction to a "hard" direction is described by

$$E_A = K_{u,1} \sin^2(\theta) + K_{u,2} \sin^4(\theta) + K_{u,3} \sin^6(\theta) \tag{1.3}$$

where $K_{u,i}$ are the anisotropy constants and θ is the angle between the magnetization and the "easy" axis.[18]

The shape anisotropy (K_{sh}) arises from the demagnetization field $(\mathcal{N})$. For a prolate ellipsoid with magnetic saturation (M_S), the shape anisotropy is

$$K_{sh} = \frac{1}{4}\mu_0 M_S^2 (1 - 3\mathcal{N}) \tag{1.4}$$

where the demagnetization field's dependence on the aspect ratio of the ellipsoid $(\alpha = c/a > 1)$ is given by

$$\mathcal{N} = \frac{1}{(\alpha^2 - 1)} \left(\frac{\alpha}{\sqrt{\alpha^2 - 1}} \cosh^{-1}(\alpha) \right) \tag{1.5}$$

For a sphere, $\mathcal{N}=1/3$, which gives the anticipated result of no shape anisotropy.[19]

In practice, this description of shape anisotropy best describes systems with uniform ordering, also known as a single domain system. However, in bulk systems, magnetically ordered regions called domains are formed to reduce the internal energy of the system by minimizing the field energy. For multidomain systems, each domain contributes its own demagnetization field, thus a relationship based on the overall aspect ratio is not applicable.

While the domain structure will align such that the system has zero magnetic moment in the absence of an applied magnetic field, the moments of the domains respond to an external magnetic field. This response is characterized by measuring the magnetization ($\vec{M}$) with respect to a varying magnetic field, known as a hysteresis loop (see Figure 1.3). At the largest applied fields, all of the magnetic moments are aligned resulting in the saturation magnetization (M_S); as the applied field is decreased, $\vec{M}$ also decreases due to domain motion. At zero applied field, the overall magnetization
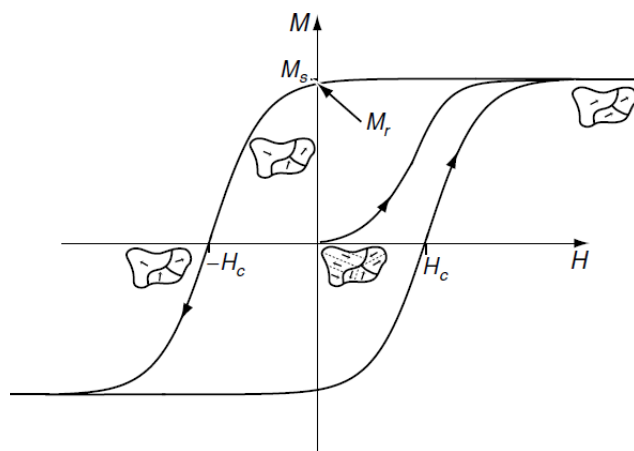
Figure 1.3: The domain structure and hysteresis loop measurements for a bulk ferromagnet, showing the magnetic saturation (M_S), magnetic remanence (M_R) and coercivity (H_C)[19]

is in remanence (M_R). Upon reversing the polarity of the field, $\vec{M}$ continues to decrease until the coercive field (H_C) where the direction of the magnetization is reversed.

The magnetic saturation of the system decreases with increasing temperature due to thermal effects on collective spin excitations known as spin waves. Because the spins are boson-like, we can use the dispersion relation $\epsilon_k = 2\hbar^2 k^2/2m$ to derive the temperature dependence of the magnetic saturation as[19]

$$M_S(T) = M(0)\left(1 - \frac{0.0587}{\nu}\left(\frac{k_B T}{2SJ}\right)^\alpha\right) \tag{1.6}$$

where $\nu = 1, 2, 4$ for a simple cubic, fcc or bcc lattice respectively, k_B is Boltzmann's constant, S is the magnitude of the spin, and J is the exchange constant. This relationship may be simplified to the form

$$M_S(T) = M(0)(1 - BT^\alpha) \tag{1.7}$$

where α is typically $3/2$ for bulk materials resulting in $B = \frac{0.0587}{\nu}\left(\frac{k_B}{2SJ}\right)^{3/2}$.[19]

1.2   Nanoparticle Magnetism

Nanoparticle magnetism is quite different from bulk magnetism. Along with the material's intrinsic magnetism, finite size effects play a significant role. In nanoparticles, surface atoms can account for up to 60% of the atoms in a nanoparticle, resulting in a large degree of disorder due to broken coordination.[20] These surface spins tend to

be oriented normal to the surface of the particles reducing the overall magnetization of the system.

Additionally, the reduced lattice size changes the overall energy landscape. When the particle size is reduced below a certain threshold, the formation of domain walls are unfavourable. The critical diameter for this condition is given by

$$D_{cr}^{sd} = \frac{72\sqrt{AK}}{\mu_0 M_S^2} \tag{1.8}$$

where A is the exchange stiffness constant (which is related to B in Equation 1.7 through S and J[19]), K is the uniaxial anisotropy constant, M_S is the magnetic saturation, and μ_0 is the magnetic permeability in vacuum.[21] For Fe_3O_4, this critical diameter is 50 nm for cubic particles and up to 76 nm for elongated nanoparticles.[22]

In a simple single-domain nanoparticle, the Stoner-Wohlfarth model can be used to describe the magnetism.[23] Based on Equation 1.4, the energy barrier to magnetic reversal for a uniaxial particle is $E = KV\sin^2(\theta)$. When a magnetic field (H) is applied, the energy becomes
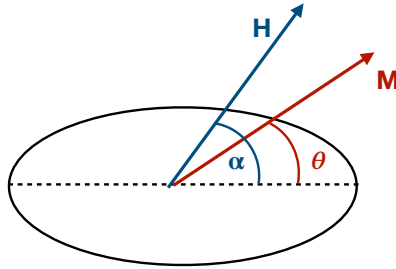
Figure 1.4: Schematic of a Stoner-Wohlfarth particle. The angle between the applied field (H) and the anisotropy (easy) axis is defined as α, while the angle between the magnetization (M) and easy axis is defined as θ.

$$E = KV \sin^2(\theta) - M_S V H \cos(\alpha - \theta) \tag{1.9}$$

where α is the angle between the applied field $(\vec{H})$ and the anisotropy (easy) axis and θ is the angle between the magnetization $\vec{M}$ and the easy axis as shown in Figure 1.4. Setting $\alpha = 0$ for a field applied along the easy axis, the difference between the maxima and minima of the energy landscape gives the energy barrier as

$$\Delta E = KV \left(1 + \frac{M_S H}{2K}\right)^2 . \tag{1.10}$$

However, this does not account for thermal effects on the system. For a set of nanoparticles at a non-zero temperature T, the magnetization will vary as a function of time (t) as

$$\frac{dM}{dt} = -\frac{1}{\tau_0} M e^{-\frac{\Delta E}{k_B T}} = \frac{M}{\tau} \tag{1.11}$$

where $1/\tau_0$ is the number of times the system attempts to surpass the energy barrier and τ is the relaxation time. By rearranging this equation, the Néel-Arrhenius Law is obtained.[24]

$$\tau = \tau_0 \exp\left(\frac{\Delta E}{k_B T}\right) \tag{1.12}$$

If there is no applied field, $\Delta E = KV$. Thus, for a fixed energy barrier, there is a

temperature where the system has sufficient energy to reverse the magnetization. This temperature is known as the blocking temperature (T_B) because for temperatures below T_B the nanoparticles magnetization is magnetically stable, while above T_B, $\vec{M}$ can reverse spontaneously. However, the determination of T_B depends on the measuring time (τ_m), since the system appears blocked for $\tau_m < \tau$. By incorporating the measuring time, the blocking temperature is described by

$$T_B = \frac{KV}{\ln \frac{\tau_m}{\tau_0} k_B} \tag{1.13}$$

For a system with an applied magnetic field, ΔE is described by Equation 1.10. By substituting this into Equation 1.12, the temperature dependence for the coercive field of a uniaxial single domain particle is obtained:

$$H_C = \frac{2K}{M_S} \left(1 - \sqrt{\frac{T}{T_B}} \right) \tag{1.14}$$

It is important to remember that Equation 1.14 was obtained by assuming the applied magnetic field was along the magnetic easy axis. While this temperature dependence holds regardless of the angle (α) between the applied field and the easy axis, the changing energy landscape described by Equation 1.9 speaks to the hysteresis loop shape changing as a function of α, as shown in Figure 1.5. Since the magnetic saturation is by definition the maximum magnetization, this parameter has no angular dependence; however both H_C and M_R are affected. At $\alpha = 0°$, the loop appears perfectly square, with $M_R/M_S = 1$ and maximum coercivity $(H_a = \frac{2K}{M_S})$. As the angle between the applied field and magnetization is increased, both the coercivity
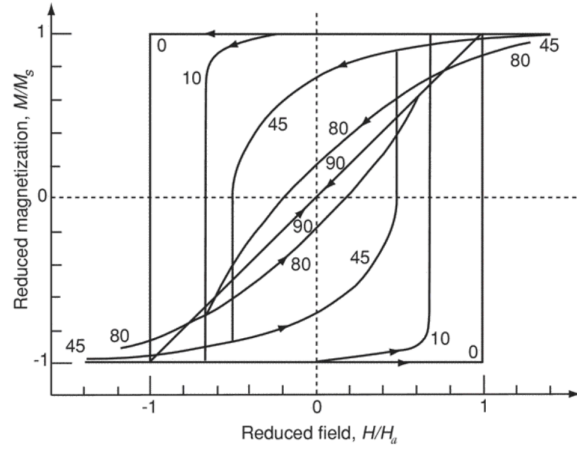
Figure 1.5: Hysteresis loops as a function of α, the angle between applied field and easy axis. The applied field, H, is normalized to the maximum coercive field ($H_a = \frac{2K}{M_S}$), while the magnetization is normalized to the magnetic saturation (M_S).[19]

and remanence decrease until $\alpha = 90°$ where $H_C = M_R/M_S = 0$.

For nanoparticle samples, measurements are typically done on an array of randomly oriented particles, rather than the single particle assumed thus far. For such a randomly oriented system, $M_R/M_S = 0.5$ and $H_C/H_a = 0.482$.[19]

However, the Stoner-Wohlfarth model assumes that the magnetization will reverse via coherent rotation. While this is the most simple reversal mode (where all spins
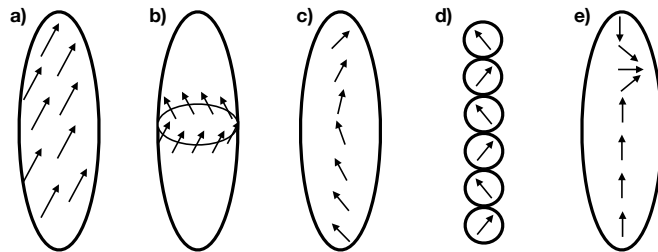
Figure 1.6: Reversal mechanisms of anisotropic particles: a) incoherent rotation, b) curling, c) fanning, d) fanning (in chain of spheres), and e) domino effect.

simultaneously rotate), it is not the only option. For anisotropic shaped particles, curling is often the most significant incoherent reversal mechanism, though buckling, fanning and domino effects are also possible (see Figure 1.6).[25] Because the reversal mode is determined by competition between the demagnetization and exchange energies, it is highly dependent on the geometry of the nanoparticles with the probability of curling increasing with aspect ratio.[26][27] When the magnetization is applied along the easy axis, a critical diameter for curling to occur can be estimated by

$$d_c = 2q \left(\frac{2}{\mathcal{N}}\right)^{1/2} \frac{A^{1/2}}{M_S} \tag{1.15}$$

where q is related to the aspect ratio of the spheroid (1.84 for a cylinder), $\mathcal{N}$ is the demagnetizing factor (with a maximum of 2π), A is the exchange constant stiffness, and M_S is the magnetic saturation. For magnetite, the critical diameter is $\sim$39 nm. As the angle between the easy axis and magnetization is increased the demagnetization factor is decreased until coherent rotation becomes energetically favourable.[28]

1.3   Magnetite

1.3.1   Structure and Properties at Room Temperature

Magnetite (Fe_3O_4) is one of the oldest known magnetic materials. It is an inverse spinel composed of tetrahedral, T_d, A-site Fe^{3+} and octahedral, O_h, B-site Fe^{2+} and Fe^{3+} with a nominal cation distribution of $(Fe^{3+})_A[Fe^{2+}Fe^{3+}]_BO_4$. However, its unusually high conductivity under ambient conditions has been interpreted as
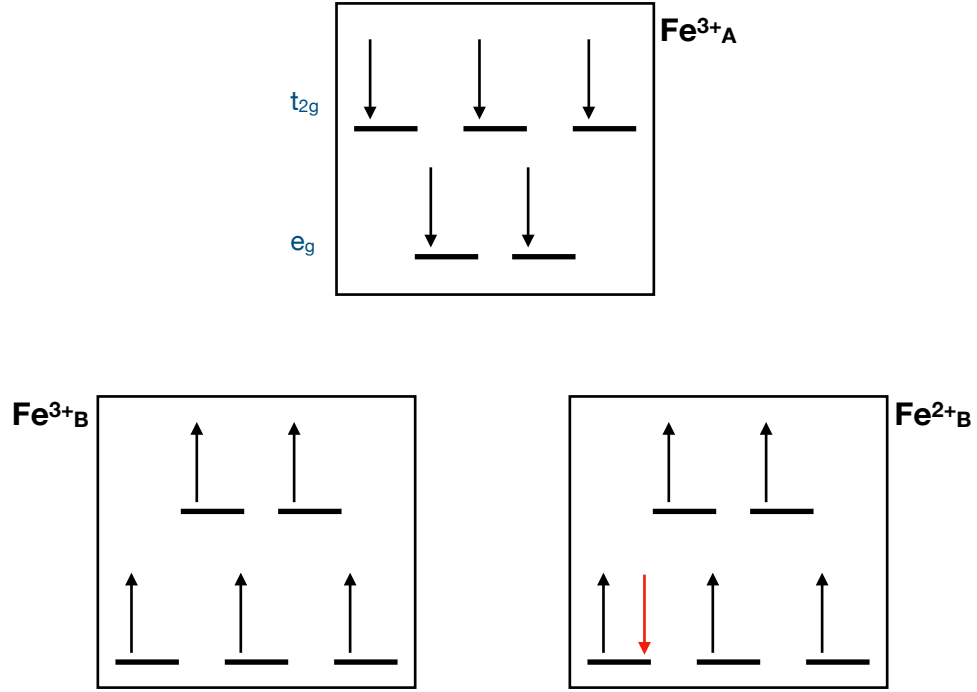
Figure 1.7: Schematic of crystal field splitting and e_g and t_{2g} occupations of Fe^{2+} and Fe^{3+} in Fe_3O_4. The t_{2g} electron that leads to the formation of a double-exchange pair is shown in red. The double exchange results in ferromagnetic coupling between B-sites, while the A and B sublattices are coupled antiferromagnetically via superexchange.

electron hopping between B-sites, resulting in an effective cation distribution of (Fe^{3+})[$Fe^{2.5+}$]$_2O_4$.[29] At room temperature the unit cell is fcc (Fd$\bar{3}$m) with a lattice spacing of 8.39 Å.[30]

Fe$_3$O$_4$ is a ferrimagnet due to the antiferromagnetic coupling of the A and B sublattices via the superexchange interaction mediated by O^{2-}. From Hund's rules, Fe^{3+} has a d^5 configuration with the d-orbital half-filled with parallel spins, while the additional electron in Fe^{2+} is anti-parallel to the other spins resulting in net moments of 5 μ_B and 4 μ_B, respectively. In Fe$_3$O$_4$, the octahedral cations are coupled via double exchange, where a ferromagnetic arrangement permits the additional t_{2g} electron to

hop between ions.[31] Since the magnetic contributions of Fe^{3+} in the A and B-sites will counteract each other, the net magnetic moment for Fe_3O_4 is 4 μ_B. A schematic of the crystal field splitting configuration is presented in Figure 1.7.

1.3.2   Verwey Transition

In 1939, Evert Verwey first reported the change in structure and electronic conductivity at 120 K that has become known as the Verwey transition.[32] At this transition temperature (T_V), the lattice shifts from a cubic to a monoclinic phase. Since the discovery of the Verwey transition, much work has been focused on characterizing the low temperature phase of Fe_3O_4 with regards to structure and charge ordering. While an approximation of the crystal structure was published in 1982 by Iizumi et al.[33], only recently has the full $C2/c$ space group been resolved for bulk Fe_3O_4.[34]

Similarly, our understanding of the low temperature charge ordering has been evolving. Verwey's original proposal of alternating Fe^{2+} and Fe^{3+} in the octahedral B sites[35] has been discarded as both experimental techniques and theoretical modelling have improved.[36][37] Recently, Senn et al. have used the predictions of electronic band structure calculations based on density functional theory (DFT) with the inclusion of Coulomb interactions (DFT+U scheme)[38] and observed shortening of B site Fe-Fe distances to introduce the concept of "trimerons".[39][40]

Trimerons are quasiparticles formed by the delocalization of t_{2g} electrons from a central Fe^{2+} ion to two acceptor ions as shown in Figure 1.8. The existence of trimerons has been corroborated by NMR experiments,[41] and using pump-probe techniques, de Jong et al.[42] have demonstrated that the existence of trimerons is
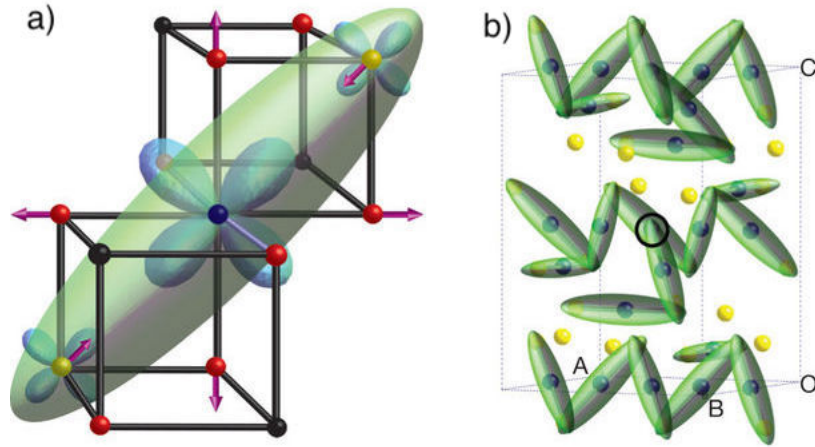
Figure 1.8: Colour online. a) Schematic of a typical trimeron where a Fe^{2+} ion (blue) shared t_{2g} electrons with Fe^{3+} ions (yellow). The changes in Fe-Fe and Fe-O bond lengths are indicated by red arrows. O^{2-} ions are shown in red and non-interacting Fe ions are black. b) Distribution of trimerons in Fe_3O_4 below T_V. Fe^{2+} ions are blue and Fe^{3+} are yellow. The black circle indicates the one Fe^{2+} that acts as an electron acceptor. Reprinted with permission from [39]. Copyright 2011 Springer Nature.

essential to the low temperature monoclinic phase. The annihilation of these quasi-particles causes the crystal lattice to return to a cubic state.

Because the Verwey transition is accompanied by changes in electronic and magnetic properties, being able to control the Verwey temperature is of great interest. High pressure measurements of powder Fe_3O_4 have determined that T_V is inversely related to isotropically applied pressure,[43][44] though it can be increased by uni-axial strain. There have been multiple reports in literature addressing the effect of strain on T_V with most studies focused on epitaxial thin films grown on a mis-matched substrate.[45][46] Recently, density of state calculations have been performed modelling the effect of biaxial strain on both $P2/c$ and Cc space groups. These cal-culations predict the distribution of trimerons to be affected by strain with those in certain directions being strengthened, while others are weakened.[47] While studies

have been done on single crystals with external uniaxial strain,[48] Fe_3O_4 nanoparticles, particularly those with uniaxial anisotropy, are an ideal system for studying the effects of internal strain on the Verwey transition in three dimensions.

Chapter 2

Experimental Methods

2.1 X-ray Diffraction

X-ray diffraction is used to characterize the crystal structure of samples. The constructive interference of x-rays scattered from electrons in a crystal lattice leads to a diffraction pattern from which the lattice spacing may be determined. This relation-
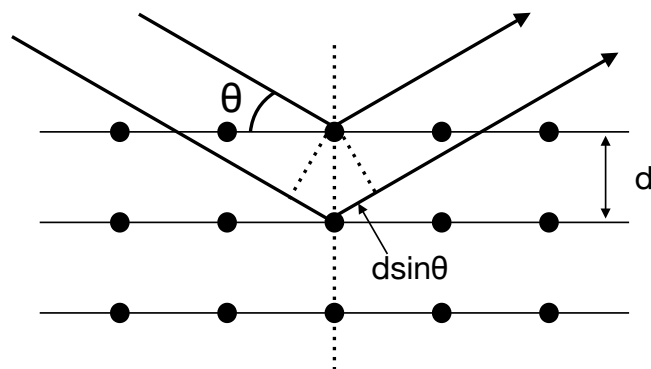
Figure 2.1: Schematic of Bragg diffraction.

ship is described by the Bragg equation

$$n\lambda = 2d_{hkl}sin\theta \tag{2.1}$$

where n is a positive integer, λ is the wavelength of the x-rays, d_{hkl} is the distance between parallel planes of atoms of family hkl, and θ is half of the scattering angle. An illustration of Bragg diffraction is located in Fig. 2.1.

For an infinite number of crystal planes, the width of the diffraction peaks is determined by instrumental factors; however, for nanoparticles, peak broadening occurs due to finite size effects. This broadening is related to the crystallite size by the Scherrer equation

$$\tau = \frac{K\lambda}{\beta cos\theta} \tag{2.2}$$

where τ is the average crystallite size, K is a dimensionless shape factor (0.9 for spherical particles), λ is the x-ray wavelength, β is the full width at half maximum (FWHM) of the intensity in radians, and θ is the Bragg angle.[49]

The reader is referred to [50] for a full treatment of the experiment and analysis. In brief, XRD patterns were collected to determine the structure of the nanoparticles. All patterns were collected using Cu-K$_\alpha$ radiation with Bragg-Brentano geometry in a Bruker D8 DaVinci (see Figure 2.2). X-rays are generated using an x-ray tube consisting of an electrically heated tungsten cathode, an anode and a Be window. A large potential difference (40 eV) between the anode and cathode causes electrons to

accelerate to the Cu anode target; when the tube current (40 mA) strikes the target, characteristic Cu x-rays and Bremsstrahlung radiation are generated.

For the room temperature measurements using a rotation stage, motorized slits were used on both the primary and secondary optics to collimate the beam, while a Ni filter was used to attenuate the Cu-K_β and Bremsstrahlung x-rays. A Lynxeye linear Si strip detector quantifies the diffracted x-rays. Dried nanoparticles samples were mounted on a zero-background quartz slide and analysis via Reitveld refinement was done FullProf.[51]

Low temperature measurements were done with the Oxford Cryosystems PheniX closed cycle refrigeration system stage. A Göebel mirror and 1 mm slit was used to collimate the primary optics, while a motorized slit was used on the secondary optics. Sequential pattern refinement was done using GSAS II incorporating both
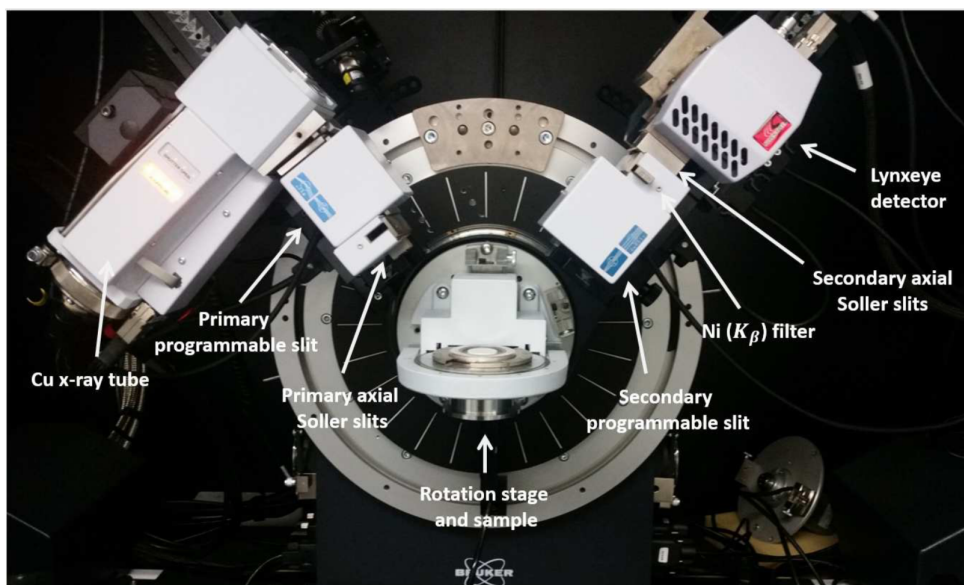
Figure 2.2: Bruker D8 DaVinci with rotation stage.

microstrain and texture.[52]

2.2 Dynamic Light Scattering (DLS) and Zeta Potential Measurement

Dynamic light scattering is used to measure the hydrodynamic radii and size distribution of particles in solution. Coherent, monochromatic light is directed through a colloid where it is scattered via Rayleigh scattering as particles undergo Brownian motion. A photomultiplier tube collects the scattered photons at a variety of angles about the sample. While a brief overview of the technique is provided below, the reader is directed to [53] for a more complete discussion.

The signal is processed with a correlator, and the resulting autocorrelation function is dependent on delay time. After subtracting the baseline, the data takes the form

$$C = e^{-Dq^2\tau} \tag{2.3}$$

where D is the diffusion constant, q is the scattering vector, and τ is the delay time. Both the scattering vector and diffusion constant depend on the experimental setup. The relationship for the scattering vector is

$$q = \frac{4\pi n}{\lambda} \sin\left(\frac{\theta}{2}\right) \tag{2.4}$$

where n is the refractive index of the suspension liquid, λ is the wavelength of the laser light, and θ is the scattering angle. Stokes-Einstein equation relates the diffusion constant to the hydrodynamic radius by

$$D = \frac{k_B T}{6\pi\eta r} \tag{2.5}$$

where k_B is Boltzmann's constant, T is the temperature of the system, η is the dynamic viscosity of the solvent and r is the hydrodynamic radius of the particles.

The zeta potential (ζ) is the electric potential between the surface of a colloidal particle and the fluid in which it is immersed. While often used as a measure of colloidal stability (a higher magnitude of ζ corresponds to a more stable system), the zeta potential also provides insight into the surface charge of particles. For this work, zeta potential was measured using electrophoresis. An electric field is applied to the sample causing movement between the fluid and its particles. Once the electric field (E) is such that the particles move with constant velocity (v), the velocity of the particles is measured using phase analysis light scattering. The electrophoretic motility of the system (μ_e) can then be calculated using

$$\mu_e = \frac{v}{E} \tag{2.6}$$

Using von Smoluchowski's classical model, μ_e relates to ζ by

$$\mu_e = \frac{\epsilon_r \epsilon_0 \zeta}{\eta} \tag{2.7}$$

where ϵ_r is the dielectric constant of the fluid, ϵ_0 is the permittivity of free space, and η is the dynamic viscosity of the fluid.[54] Thus the zeta potential can be calculated using

$$\zeta = \frac{\eta v}{\epsilon_r \epsilon_0 E} \tag{2.8}$$

where v and E are determined experimentally.

DLS measurements were done on suspensions of nanoparticles in DI H_2O using a Photocor Complex system at variable angles. Zeta potential measurements were done with a Horiba Nano-Partica SZ-100 series instrument on the same samples. Both measurements were acquired a room temperature.

2.3   Mössbauer Spectroscopy

The Mössbauer effect, discovered by Rudolf Mössbauer in 1958, describes the recoil-free absorption and emission of photons of atomic nuclei in a solid.[55] Mössbauer spectroscopy uses this effect to probe the local electronic and magnetic environment of atoms in a sample. For a full reference, the reader is referred to [56].

When a free nuclei decays from excited state E_e to ground state E_g where $E_0 = E_e - E_g$, a photon with energy is emitted. From conservation of momentum, the nuclei experiences a loss in energy due to recoil expressed by

$$E_R = \frac{E_\gamma^2}{2M_N c^2} \tag{2.9}$$

where E_γ is the energy of the emitted photon, M is the mass of the recoiling object and c is the speed of light. From conservation of energy, the energy of the emitted γ-ray is given by

$$E_\gamma = E_0 - E_R \tag{2.10}$$

For recoil-free absorption to occur, the incoming photon must have enough energy to compensate for recoil, i.e. $E_\gamma = E_0 - E_R$. From Heisenberg's uncertainty principle, the uncertainty in the energy of both the emitted and absorbed γ-ray is related to the half-life of the excited state by $\Gamma_{nat} = \hbar/\tau_{1/2}$. In order to have recoil-free absorption and emission, there must be overlap between the energies of the absorbed and emitted photons, so $\Gamma_{nat} > 2E_R$.

For free nuclei, E_R is typically orders of magnitude larger than Γ_{nat} which means that the probability of resonant fluorescence is extremely low; however, if the nucleus is embedded in a matrix, the recoil energy may be transferred to the matrix. Since the mass of the matrix is significantly larger than that of an individual nuclei, E_R is reduced provided that the energy does not create a lattice excitation (phonon), thus increasing the probability of recoil-free absorption and emission. The probability of a zero-phonon event is given by the recoilless fraction as

$$f = exp[-E_\gamma^2 \left\langle x^2 \right\rangle / (\hbar c)^2] \tag{2.11}$$

where $\langle x^2 \rangle$ is the mean square vibrational amplitude of the emitting atom in the direction of the emitted photon.[56] This is related to the Debye-Waller factor where the solid's phonon modes are described by the Debye model.[57]

A Mössbauer spectra is collected by measuring the transmission of Doppler-shifted γ-rays through a sample. For the study of ^{57}Fe, a radioactive ^{57}Co source is moved relative to the sample producing Doppler-shifted γ-rays with energies around E_0 (see decay scheme in Figure 2.3; when the energy of the incoming γ-ray excites a nuclear transition in the sample, absorption occurs; a Mössbauer spectrum is thus a measure of transmission as a function of the Doppler-shifted energy.

Mössbauer spectroscopy is useful because it provides information about the electron density, electric field gradient and hyperfine field at the nucleus via hyperfine interactions. When combined, these characteristics provide valuable insight into the composition, bonding and magnetism of samples. The relationship between the hy-
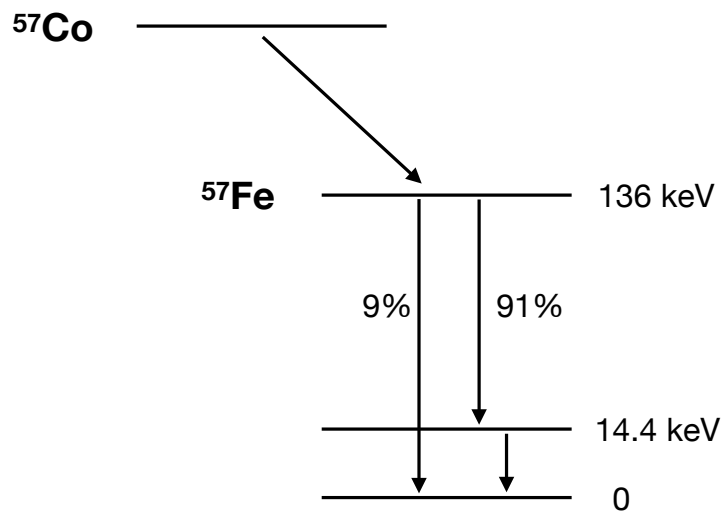
Figure 2.3: The decay scheme of ^{57}Co.
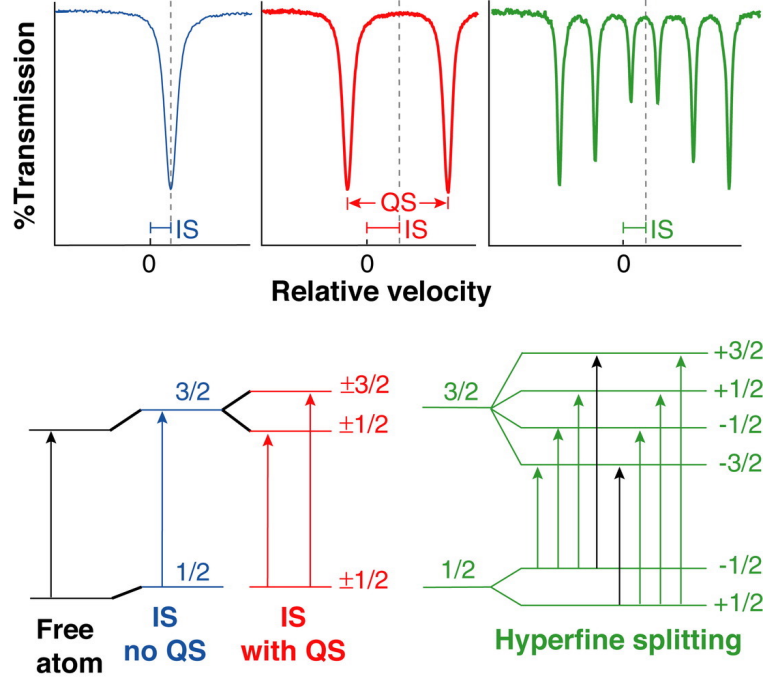
Figure 2.4: Hyperfine parameters and their effect on the Mössbauer spectrum. Forbidden transitions in the magnetic hyperfine splitting are shown in black.[58]

perfine parameters and the Mössbauer spectra is shown in Figure 2.4.

The isomer (centroid) shift (δ) is the result of an intrinsic component (δ_I) and and the second-order Doppler shift (δ_{SOD}) where $\delta = \delta_I + \delta_{SOD}$. The intrinsic isomer shift is caused by in differences in s-electron density between the source and the absorber

$$\delta_I = \frac{2\pi}{5} Z e^2 \{ |\psi_s(0)_A|^2 - |\psi_s(0)_S|^2 \} \{ R_e^2 - R_g^2 \} \tag{2.12}$$

where Z is the atomic number, e is the charge of an electron, $|\psi_s(0)_A|^2$ and $|\psi_s(0)_B|^2$ are the s-orbital electron densities of the absorbing nuclei and source nuclei respectively, and R_e and R_g are the radii of the nuclei in the excited and ground states. It is important to note that $R_e < R_g$ for ^{57}Fe; this means that an increase in the s-orbital

density leads to a lower isomer shift.[59] While both ^{57}Co and ^{57}Fe have the same number of s-orbital electrons, the screening effect of the d-electrons combined with different chemical environments leads to different electron densities between source and absorber. Since the isomer shift is sensitive to changes in the d-orbital electrons, this parameter is useful in distinguishing Fe^{2+} from Fe^{3+}. The second-order Doppler shift is a function of the mean-squared velocity of the absorbing atom ($\langle v^2 \rangle$) by

$$\delta_{SOD} = -E_\gamma \frac{\langle v^2 \rangle}{2c^2} \tag{2.13}$$

Since $\langle v^2 \rangle$ is proportional to the kinetic energy of the absorbing nuclei, δ_{SOD} will decrease with increasing temperature. This temperature dependence creates the need for δ to be reported relative to a standard at a set temperature. The convention is to report δ relative to α-Fe at room temperature (300 K).

The quadrupole splitting of the Mössbauer spectra speaks to the electric field gradient. Only states with the nuclear quantum number $I > 1/2$ will have a non-zero quadrupole moment Q. When exposed to an electric gradient field, $2I + 1$ magnetic substates (m_I) form, however, states with $|m_I|$ remain degenerate. In the case of ^{57}Fe, $I = 3/2$ results in a doublet . The energy of this splitting is given by

$$E_Q = \frac{eQV_{zz}}{2}\sqrt{1 + \frac{\eta^2}{3}} \tag{2.14}$$

where $V_{zz} = \partial^2 V/\partial z^2$ is the principal component of the electric gradient field tensor, and η is the asymmetry parameter given by

$$\eta = \frac{V_{xx} - V_{yy}}{V_{zz}} \tag{2.15}$$

where V_{xx} and V_{yy} are the off diagonal elements and $0 \leq \eta \leq 1$.

The interaction between the nuclear spin $\vec{I}$ and magnetic moment $\vec{\mu}$ via Zeeman interactions is described by the Hamiltonion

$$\mathcal{H} = -\vec{\mu} \cdot \vec{B_{hf}} = -g_N \mu_N \vec{I} \cdot \vec{B_{hf}} \tag{2.16}$$

where g_N is the nuclear Landé factor, μ_N is the nuclear magneton, and B_{hf} is the induced magnetization. The energies for the nuclear levels are then proportional to the magnetic substates (m_I) and may be expressed as

$$E_M = -g_N \mu_N m_I B_{hf} \tag{2.17}$$

For the transition in ^{57}Fe from ground state $I = 1/2$ to excited state $I = 3/2$, the selection rules of $\Delta I = 1$ and $\Delta m_I = 0, \pm 1$ allow six transitions as illustrated in Figure 2.4, resulting in a sextet. For a randomly oriented powder, the relative transmission probabilities, determined by the Clebsch-Gordon coefficients, are 3:2:1:1:2:3.

For the Mössbauer experiments in this thesis, a ^{57}Co source in a Rh matrix was mounted on a Wissel MDU MR-360 transducer. A Wissel DFG-1200 digital function generator induced a triangular wavefunction to produce Doppler-shifter γ-rays that are directed through the sample. The transmitted γ-rays are quantified using a LND model 45431 Ar/Xe proportional counter and amplified before reaching a ORTEC

single channel analyzer (SCA). The discriminators on the SCA are adjusted to allow only the 14.4 keV γ-rays to be counted. This signal is then sent to a computer with an ORTEC multi-channel scaler (MCS) where the data is sorted with respect to the drive velocity. A Janis SHI-850 closed cycle refrigerator was used to collect spectra from 10 K to 300 K in order to determine the temperature dependence of hyperfine parameters.

2.4   Electron Microscopy

Electron microscopes are invaluable tools in the analysis of nanoparticles. Transmission electron microscopy (TEM) is an imaging and diffraction technique that focuses a high energy beam of electrons through the sample. Transmitted electrons may be used to form a bright field image of the sample. Since the beam passes through the sample, the contrast of the final image is a result of electron absorption. Thus TEM bright field images provide information about sample thickness and the atomic number (Z) of the atoms as well as overall morphology.

In contrast with TEM, scanning electron microscopes (SEM) use a highly focused electron beam to raster across the surface of a sample. Since the electron beam does not need to transmit through the sample, SEM may be used to image thicker samples than TEM. As the electrons interact with the sample, both electrons and x-rays are produced. Detectors collect the secondary and backscattered electrons, and the signals are assembled into images. The secondary electron image is useful in determining sample size and morphology, while the image produced from the backscattered electrons provides information about the atomic cross-section of the sample.

Nanoparticles were suspended in ethanol and dropped onto a 200-mesh carbon-coated copper grid. SEM images were collected on a FEI Nova NanoSEM 450, while TEM images were collected on a FEI Talos F200X S/TEM at the Manitoba Institute of Materials (MIM). The SEM was operated at 5 keV, while the TEM was operated at 200 keV. ImageJ was used for particle size distribution and shape analysis.[60]

2.5   Magnetometry and Susceptometry

The overall magnetic properties of nanoparticles were determined using a magnetometer. In this thesis, measurements were obtained using a superconducting quantum interference device (SQUID) magnetic property measurement system (MPMS) from Quantum Design. This instrument consists of four key superconducting components: the superconducting magnet, the superconducting detection coils, the superconducting shield, and the SQUID device itself; all components are located within a liquid helium dewar. The superconducting magnet is a solenoid that can produce magnetic fields up to ± 5 T depending on the applied current. At the centre of the solenoid, the superconducting detection coils wrap around the sample chamber in a second-order gradiometer configuration. This configuration means that the current within the detection coils are constant if the external magnetic field is constant. As the sample is moved through the magnetic field, the change in magnetic flux induces a current in the detection coils. This induced current is transmitted then through superconducting wires to allow for inductive coupling to the SQUID detector.[61]

The SQUID device consists of two Josephson junctions in the loop's current and

converts the input current to a proportional output voltage. Due to the high degree of sensitivity in the SQUID, this device is isolated from the superconducting magnet by a superconducting shield. For each data point, the voltage is measured relative to the sample's position; this plot is then fit to a dipole via an iterative regression to obtain a quantification of measured magnetization.

All measurements for this thesis were acquired using a standard transport, which physically moves the sample through the magnetic field. The sample space is maintained at low pressure and filled with helium gas with heaters around and above the sample area to allow for precise temperature PID control. Measurements were performed on both powder samples and nanoparticles dispersed (and aligned if required) in GE varnish.

DC susceptibility (χ_{DC}) was acquired under both field cooled (FC) and zero field cooled (ZFC) conditions where a small field (typically 5 mT) was applied and the temperature was varied from 10 K to 400 K. Prior to the ZFC measurement, the magnet was reset and the shield was degaussed to remove any remanent magnetic fields.

Hysteresis loops were also acquired by measuring the magnetization of the sample (M) as a function of applied field ($\mu_0 H$) for fixed temperatures between 10 K and 400 K. These measurements provide key characteristics of the sample including magnetic saturation (M_S), coercivity (H_c) and remanent field (M_R).

While DC susceptibility and hysteresis loops provide information about the static magnetism of a sample, AC susceptibility measurements give insight into the dynamic magnetism since these measurements take place on a much shorter time scale. After

cooling in zero magnetic field, a very small (0.25 mT) AC magnetic field was applied and the temperature was varied as in the DC susceptibility measurement; the acquired signal is of the form

$$\chi_{AC}(\nu, T) = \chi'_{AC}(\nu, T) - i\chi''_{AC}(\nu, T) \tag{2.18}$$

where $\chi'_{AC}(\nu, T)$ and $\chi''_{AC}(\nu, T)$ are the in-phase and out-of-phase components respectively, to the AC field with frequency ν.

2.6   X-ray Absorption Spectroscopy and Magnetic Circular Dichroism

X-ray spectroscopic techniques are invaluable to due their ability to probe individual elements. For this work, x-ray absorption spectroscopy (XAS) and x-ray magnetic circular dichroism (XMCD) were used to detect changes in oxidation state, coordination and magnetism of specific elements with both temperature and magnetic field. Both of these techniques require a high flux of high energy x-rays, thus synchrotron x-rays are ideal. These x-rays are produced when high energy electrons are accelerated in a circular path using electromagnetic field. The synchrotron x-rays are tuned to the desired energy and polarized using a combination of mirrors and undulators.[62]

In an XAS experiment, monochromatic x-rays are absorbed to excite a core electron in the element of interest. The excitation of of a core electron to the valence band only occurs if the energy of the incoming photon exceeds the characteristic binding energy, thus making XAS an element-specific technique. From dipole selection rules
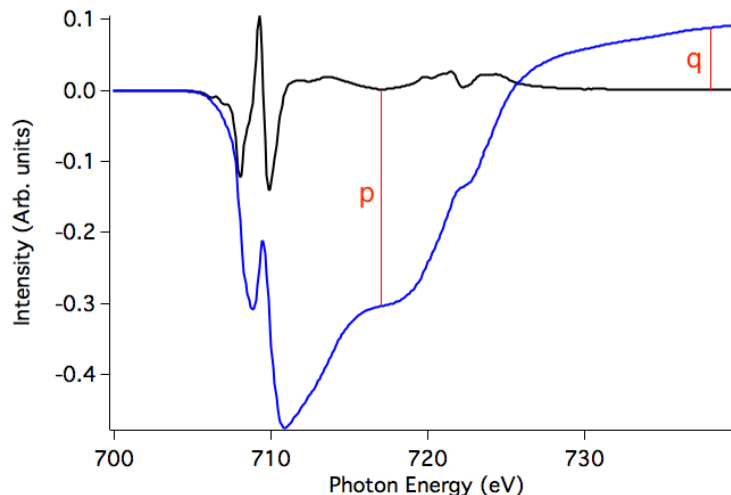
Figure 2.5: Colour online. Example of Fe L-edge XMDC spectra (black) and integrated area (blue). Lines at 717 eV and 738 eV mark p (integrated intensities over the L_3 edge) and q (integrated intensities over the combined L_2 and L_3 edges) used in sum rules analysis.

requiring $\Delta L=\pm 1$ and $\Delta S=0$, s-state electrons can only reach a final p-state, while p-state electrons can only reach final d- or s-states.

While XAS is extremely useful, magnetic experiments benefit most from the use of polarized light. Because of the selection rules for x-ray absorption, transitions will occur with different probabilities for left and right circularly polarized light as a result of the different angular momenta of the incoming photons. The XMCD signal is the difference in absorption between the two polarities. This is a direct measure of the difference between the spin up and spin down valence states which is proportional to the overall magnetization. Because the L_2 and L_3 edges correspond to opposite spin orbit couplings ($l + s$ and $l - s$ respectively), the resulting spin polarization is antiparallel at the two edges. While the x-ray does not directly interact with the electron spin, an indirect spin-orbit interaction may affect the measured intensities

between the two edges. As a result, information about the spin moment (m_s) and orbital moment (m_l) can be obtained via sum rules analysis via $m_l/m_s = 2q/(9p-6q)$ where p and q are the integrated XMDC intensities over the L_3 and combined L_2 and L_3 edges respectively.[63] An Fe L-edge XMCD spectra and integrated area are presented in Figure 2.5.

X-ray absorption spectroscopy (XAS) and x-ray magnetic circular dichroism (XMCD) measurements were done at beamline 4-ID-C of the Advanced Photon Source in a liquid helium cryostat. Powder samples were mounted on carbon tape onto a cold finger in a 7 T (maximum) field magnet oriented at a grazing angle ($\sim$30°) to the applied field and x-ray direction. Spectra were collected in total electron yield (TEY) mode with the x-ray circular polarization alternated; the XAS spectra is the sum of the two polarizations, while the XAS is the difference. XMCD spectra are normalized to the XAS spectra. Artifact free (AF) XMCD spectra are an average of both field polarity measurements to remove non-magnetic artifacts from the spectra. XAS simulations were performed using Crispy.[64]

2.7 Hyperthermia

Hyperthermia measurements were done using a 2.4 kW Ambrell Easyheat and a FLIR AX8 infrared camera. To characterize the heating response, temperature measurements were acquired with respect to time while the AC magnetic field was applied. The specific loss power (SLP) is a measure of the sample's heating efficiency; this parameter was calculated using
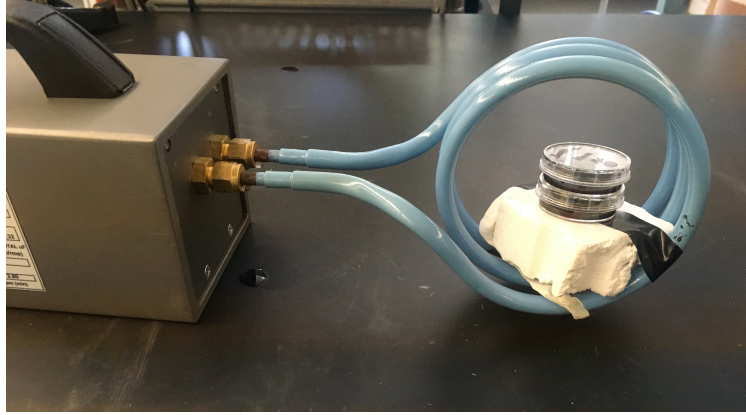
Figure 2.6: Hyperthermia setup for spherical nanoparticles.

$$SLP = C\frac{m_s}{m_p}\frac{\Delta T}{\Delta t} \tag{2.19}$$

where C is the specific heat of the solvent (4.186 J/g°C for water), m_s is the mass of the solvent, m_p is the mass of the nanoparticles, and $\Delta T/\Delta t$ is initial change in temperature with respect to time.[65]

To characterize the heating response of the spherical nanoparticles, 2 ml of 30 mg/ml solutions were added to a 35 mm polystyrene dish and the AC magnetic field (191 kHz 15.8 kA/m) was applied. Since the purpose of this measurement was to determine the temperature achieved during the biofilm test, only one concentration and field was tested. Because the concentration is high, interparticle interactions can play a role, thus the direction of the applied field needs to be specified. For this work the applied field is parallel to the surface of the polystyrene dish as shown in Figure 2.6.

To determine the heating efficiency of Fe_3O_4 nanorods, suspensions of various concentrations were prepared in water and the effect of the AC magnetic field was
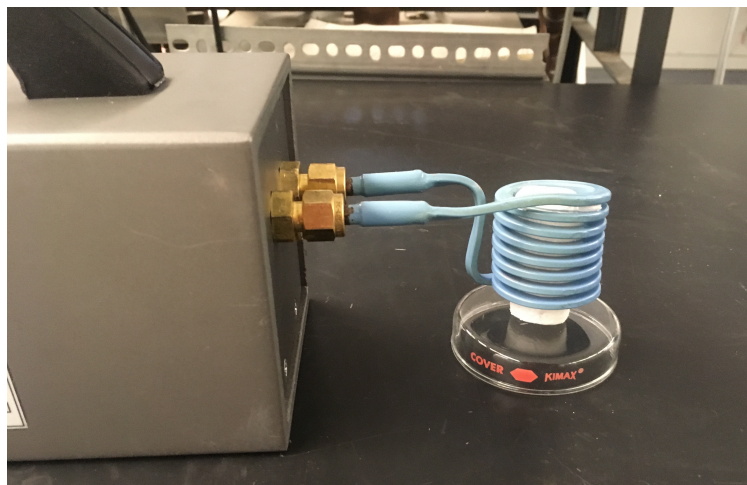
Figure 2.7: Hyperthermia setup for Fe_3O_4 nanorods.

tracked. For the nanorods, 1 ml of the desired concentration was tested as shown in Figure 2.7.

2.8 Biofilm Test

Tryptic soy broth (TSB) and tryptic soy agar (TSA) were used to culture MRSA ATCC (33592). After culturing on agar plates, an initial bacterial suspension was prepared by suspending several colonies in phosphate buffer solution (PBS; pH 7.4, 0.05 M) at an equivalent density to a 0.5 McFarland standard. This suspension was diluted 100 times in PBS, then 15 μl of the dilution was further diluted into 45 ml of TSB. After incubation for 18 h at 37°C the concentration of bacteria reached 10^8 CFU/ml. The bacterial solution was diluted 1000 times into TSB with 1% glucose. To prepare the biofilms, 2 ml of this solution was added to 35 mm polystyrene dishes and incubated 24 h at 37°C.

Prior to treatment, the bacterial solution was poured off and the films were gently
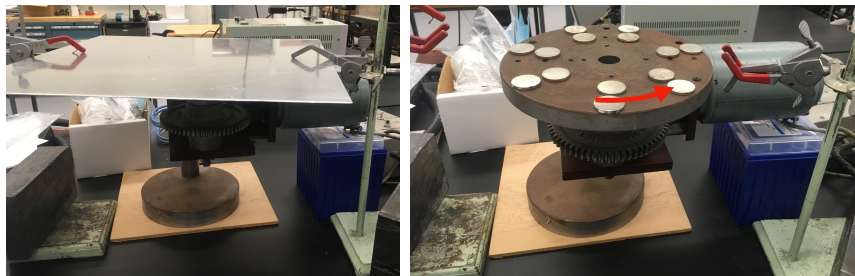
Figure 2.8: Rotating magnetic field setup with platform (left) and without platform (right). The biofilm dishes are placed on the platform above the rotating magnets.

irrigated thrice with 200 μl DI H_2O to remove planktonic bacteria. 2 ml of treatment solution was added to each film and the desired treatment condition was applied for 15 min. Treatment solutions consisted of 30 mg/ml spherical (either small or large) iron oxide nanoparticles suspended in DI H_2O; blank DI H_2O was used as a control solution. Three treatment conditions were tested: ambient conditions, a low frequency rotating magnetic field, and a high frequency alternating current (AC) magnetic field.

The rotating magnetic field consisted of neodymium permanent magnets rotating at 21 mHz under a platform containing the MRSA biofilms as presented in Figure 2.8. The AC magnetic field setup consisted of a 2.4 kW Ambrell Easyheat operating with a 191 kHz 15.8 kA/m magnetic field. The biofilms were placed inside the workhead coil such that the applied field is perpendicular to the surface of the film (see Figure 2.6) to maximize the effect of interparticle interactions.

After treatment, the treatment solution was poured off and the films were gently irrigated six times with 200 μl DI H_2O to remove planktonic bacteria and debris. After the final wash, biofilms were allowed to dry under ambient conditions then scraped into 3 ml PBS. The solution containing the removed biofilm was serially diluted in PBS

and 50 μl of each dilution was plated on TSA plates and incubated at 37°C. After 24 h, bacterial colonies were enumerated. To ensure complete tracking of bacteria, both the treatment solutions and the DI water used for washing were enumerated following the same procedure. All tests were done in triplicate. Logarithmic reduction of bacteria was determined using $\log_{10}(A/B)$ where A was the the number of bacterial colonies in the control and B was the number of colonies in the particular treatment.

Chapter 3

Iron oxide nanoparticles to treat infection

3.1 Introduction

A recent study by the World Health Organization has revealed that antimicrobial resistance has become a global health-care problem.[66] Increasingly resistant microorganisms have created a critical need for innovative solutions as the present methods using antibiotics are failing. One of the largest concerns in a hospital setting is the formation of biofilms on reusable devices such as catheters and endoscopy tubes. Biofilms are complex synergistic systems formed by the aggregation of microbes within a extra-
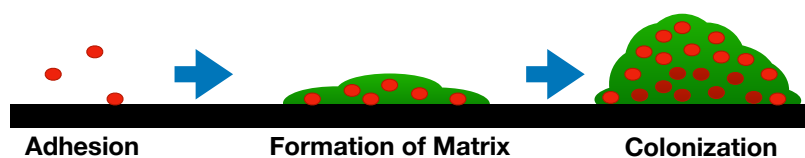
Figure 3.1: Colour online. Schematic of biofilm formation. Initially microbes (red) adhere to surface and form a protective extracellular matrix (green). As the bacteria reproduces and the biofilm becomes thicker, underlying bacteria become dormant (dark red).

cellular matrix. Typically formed at a solid-liquid interface (see Figure 3.1), biofilm constituents become more dormant as a function of depth, since nutrients become less available.[67] For bacterial films, this poses a challenge; traditional antimicrobial treatments rely on metabolization and are inefficient on dormant bacteria requiring a significantly higher dose to ensure eradication.[68]

In recent years, iron oxide nanoparticles have attracted significant attention for their uses in biomedical applications such as magnetic resonance imaging, hyperthermia and drug delivery.[69] These nanoparticles are appealing because they are non-toxic to humans and highly modifiable: Morphology and surface chemistry can be tailored to suit the desired application. In this chapter, two sizes of spherical iron oxide nanoparticles (coated with a thin coating of SiO_2 to reduce aggregation) were used to treat MRSA biofilms. While previous studies of iron oxide nanoparticles have shown no kill in planktonic bacteria,[70] we aim to demonstrate how these particles can be manipulated to disrupt biofilms.

3.2 Nanoparticle Synthesis

To synthesize small spherical nanoparticles, 8.67 g $FeCl_3 \cdot 6H_2O$ and 3.14 g $FeCl_2 \cdot 4H_2O$ were dissolved into 25 ml of 0.4 M HCl. The Fe solution was added dropwise into 250 ml of 1.5 M NaOH over 30 minutes. The nanoparticles were isolated using a strong magnet and washed thrice with DI H_2O and once with 0.01 M HCl. The nanoparticle solution was brought to a total volume of 190 ml using DI H_2O.

To synthesize large spherical nanoparticles, 8.11 g $FeCl_3 \cdot 6H_2O$ and 2.98 g $FeCl_2 \cdot 4H_2O$ were dissolved into 150 ml of DI H_2O and the solution was heated to 74°C.
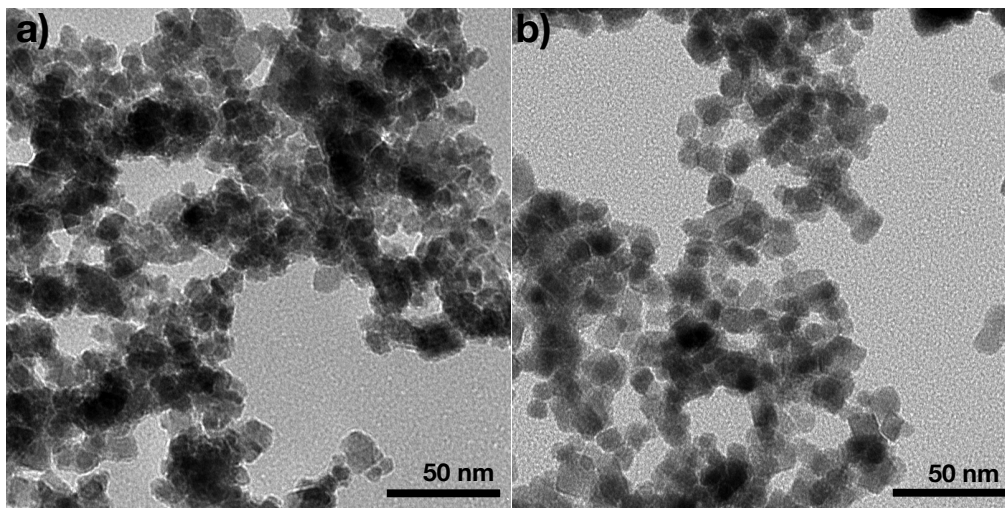
Figure 3.2: Transmission electron microscope images of a) 8 nm (small) and b) 11 nm (large) particles.

150 ml of 1.5 M NaOH was rapidly added to the Fe solution and stirred under heated condition for 1 hour. The nanoparticles were isolated using a strong magnet and washed thrice with DI H_2O and once with 0.01 M HCl. The nanoparticle solution was brought to a total volume of 190 ml using DI H_2O.

To silica coat the nanoparticles samples, 160 ml ethanol and 4 ml NH_4OH were added to the 190 ml particle solution and stirred for 5 min. 5 g TEOS was added dropwise. The mixture was stirred at room temperature for 16 hours, then washed with DI H_2O.

3.3 Characterization of spherical nanoparticles

Transmission electron microscope (TEM) images of both the large and small iron oxide nanoparticles are located in Figure 3.2. ImageJ analysis was done on TEM images to ascertain size distributions (see Figure 3.3). Each size distribution (Figure 3.3)
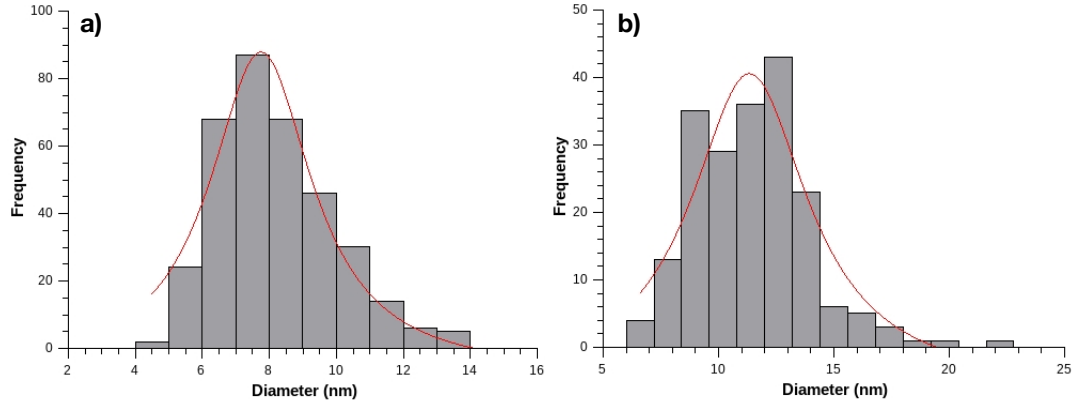
Figure 3.3: Size distributions for a) 8 nm and b) 11 nm particles determined from ImageJ analysis fit with Lorentzian distribution (red line).

was fit with a Lorentzian. From the fit results, the diameters of the two samples are 8±3 nm and 11±5 nm. Based on this analysis, the large and small spherical nanoparticles will be referred to as 8 nm and 11 nm. Zeta potential measurements on dilutions of 8 nm and 11 nm particles in DI H_2O yielded surface potentials of -33 ± 3 meV and -21 ± 3 meV respectively. These values indicate that both samples can form stable suspensions in H_2O.[54]

X-ray diffraction patterns of both the 8 nm and 11 nm iron oxide nanoparticles acquired under ambient conditions are shown in Figure 3.4. From Reitveld refinement, both samples have a $Fd\bar{3}m$ spinel structure consistent with γ-Fe_2O_3 or Fe_3O_4. The slight swell in the background $\sim22°$ indicates the presence of small amount of SiO_2 in both samples.[71] The lattice parameters of the 8 nm and 11 nm particles are 8.385±0.001 Å and 8.374±0.001 Å respectively. Since the bulk lattice parameter of γ-Fe_2O_3 is known to be 8.336 Å and for Fe_3O_4 it is 8.397 Å,[19] these results suggest non-stoichiometric Fe_3O_4. From Scherrer broadening, the volume-weighted crystallite sizes are 5.92±0.08 nm and 7.5±0.1 nm for the 8 nm and 11 nm particles respectively.
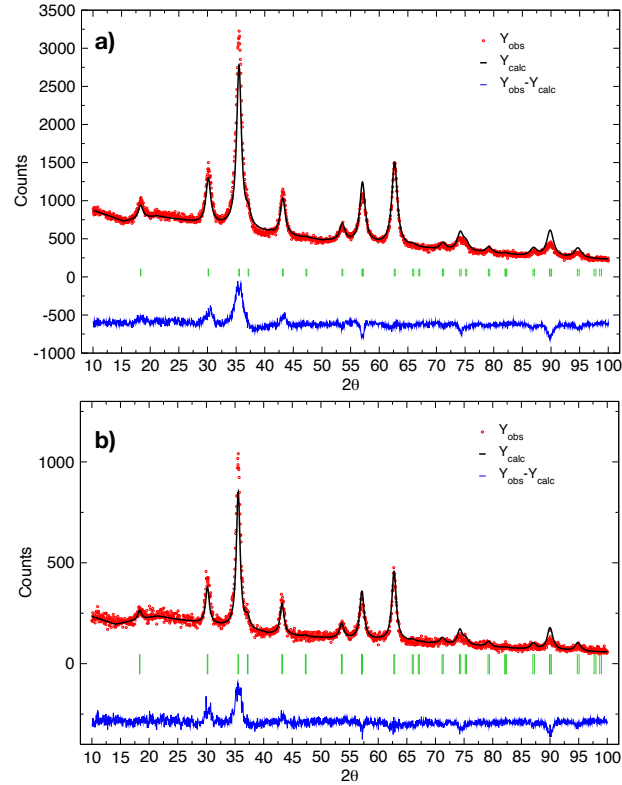
Figure 3.4: Powder x-ray diffraction patterns of a) 8 nm nanoparticles and b) 11 nm nanoparticles, with the results of the refinement (black line). The green Bragg markers index the $Fd\bar{3}m$ structure while the blue line is the residuals of the refinement.

The mismatch between the observed data and fit (visible in the residuals) is consistent with a small amount of strain in the samples expected due to the nanosize nature of the iron oxide nanoparticles.

Hysteresis quarter-loops were used to characterize the magnetic response of 8 nm and 11 nm spherical particles as shown in Figure 3.5. The 8 nm spheres have a magnetic saturation of 40.7 ± 0.8 Am^2/kg, while the 11 nm spheres have a magnetic saturation of 52 ± 1 Am^2/kg. This increase in saturation with nanoparticle size reflects the decrease of disordered surface spins. The absence of a coercive field confirms both
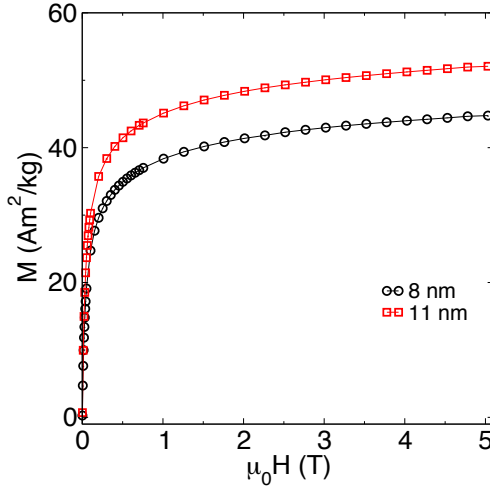
Figure 3.5: Magnetic response of 8 nm (black circles) and 11 nm (red squares) spherical nanoparticles as a function of applied field.

samples as superparamagnetic.

Mössbauer spectroscopy at 50 K was used to measure the local coordination of ^{57}Fe ions. Both spectra are primarily composed of two sextets denoted as components A and B, while the 8 nm particles have an additional sextet (C) described in Table 3.1. For the 11 nm particles, the distinct hyperfine fields of 52.55±0.08 T and 50.46±0.09 T

Table 3.1: Hyperfine parameters of 50 K Mössbauer spectra of 8 nm and 11 nm spherical nanoparticles.

Sample	Site	δ (mm/s)	Γ (mm/s)	Δ (mm/s)	B_{hf} (T)	Relative Area (%)
8 nm	A	0.49±0.01	0.23±0.02	-0.03±0.02	51.5±0.1	24
	B	0.417±0.009	0.29±0.04	0.01±0.01	49.5±0.1	48
	C	0.66±0.003	0.49±0.05	-0.18±0.05	46.7±0.3	28
11 nm	A	0.484±0.007	0.22±0.02	0.01±0.01	52.55±0.08	33
	B	0.432±0.006	0.32±0.03	-0.03±0.01	50.46±0.09	67
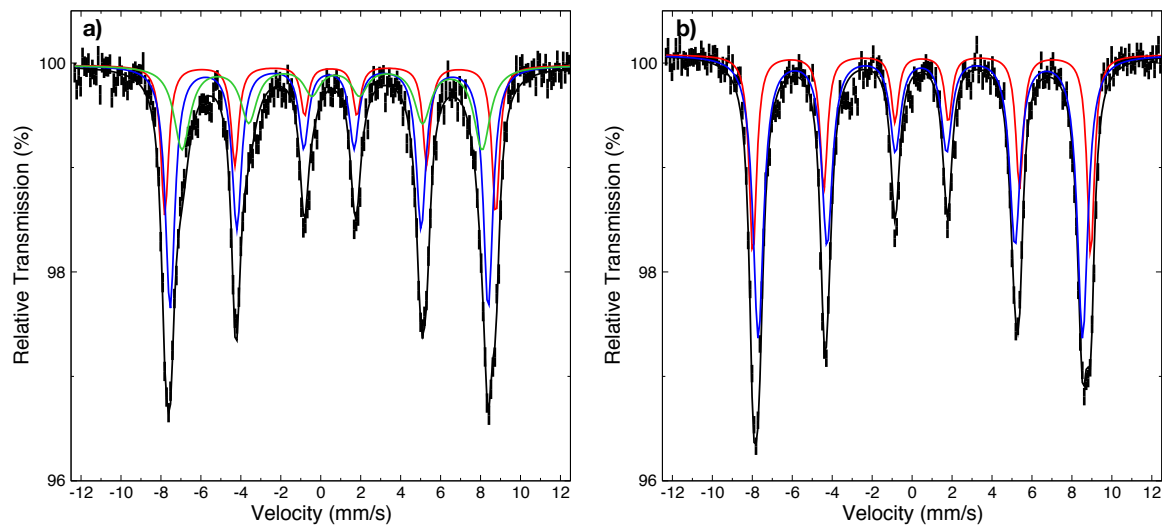
Figure 3.6: Mössbauer spectra of a) 8 nm and b) 11 nm particles at 50 K. Black markers are collected data, while black line is the fit. Red and blue sextets are components A and B, respectively, while the green is component C.

are consistent with Fe_3O_4, rather than the overlapping B_{hf} expected for γ-Fe_2O_3.[72] This conclusion is supported by the 1:2 absorption of A and B components. For the 8 nm particles, components A and B follow the same behaviour as the 11 nm with B_{hf} of 51.5±0.1 T and 49.5±0.1 T and a relative absorption of 1:2. Component C does not appear in the 11 nm particles; however, the relatively large quadrupole splitting (Δ=-0.18±0.05 mm/s) speaks to broken or distorted coordination. Combined with the large line width of 0.49±0.05 mm/s, we attribute component C to a large degree of disorder at the nanoparticles' surface. This is consistent with the increase in surface area as a result of the smaller size determined from both XRD and TEM.

Heating curves were acquired for both the 8 nm and 11 nm particles (Figure 3.7). The 8 nm particles have a calculated SLP of 4.6±0.5 W/g and an observed 9.8±0.2°C increase in temperature after 15 min (the duration of the biofilm treatment). In
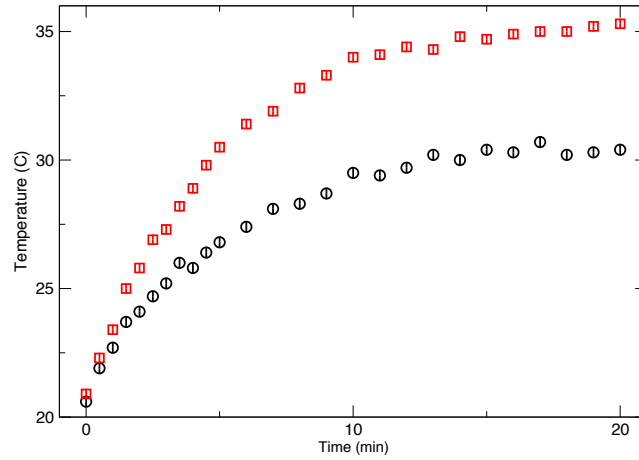
Figure 3.7: Heating curves of 8 nm (black circles) and 11 nm (red squares) nanoparticles in a 191 kHz, 15.8 kA/m AC magnetic field.

comparison, the 11 nm particles have an SLP of 6.2±0.4 W/g and a 13.8±0.2°C increase in temperature in the same time period. While neither system increases the solution temperature beyond the 37°C used during bacterial incubation, the large amount of energy transferred to the solution reveals the surface temperature of the nanoparticles to be very high. The SLP is a measure of the instantaneous heat transfer per gram of nanoparticles. We can rearrange the general heat transfer equation, $\Delta Q/t = mc_P(\Delta T/t)$, where $\Delta Q/t$ is the heat transferred with respect to time, m and c_P are the mass and heat capacity of the Fe_3O_4 nanoparticles, and $\Delta T/t$ is the temperature increase with respect to time to SLP=$c_P\Delta T/t$ where $\Delta T/t$ is the rate of temperature increase. Using $c_P = 0.65$ J/g°C for Fe_3O_4,[73] the rate of temperature increases are 7.1°C/s and 9.5°C/s, for the 8 nm and 11 nm particles respectively. If these rates are constant for the first 30 s, the nanoparticles will increase by 213°C and 285°C for 8 nm and 11 nm, respectively.

3.4 Bacterial reduction of MRSA biofilms

The results of the biofilms tests using 8 nm and 11 nm particles are presented in Figure 3.8. While bacterial results are traditionally reported in CFU/ml, the different volumes associated with the biofilm, treatment solution and washing solution make direct comparisons difficult using this convention. Instead we report the results in total CFU, since it is the reduction we are interested in.

For both sizes of nanoparticles, significant logarithmic reduction is observed in the treated biofilms compared to the controls. Under ambient conditions the logarithmic reduction for 8 nm and 11 nm particles are 2.5±0.5 and 2.7±0.4, respectively. These results are consistent with those observed by Niemirowicz et al.[74] using aminosilane-coated iron oxide nanoparticles. When exposed to a low frequency rotating magnetic field, the 8 nm particles resulted in a reduction of 3.6±0.4 $\log_{10}$, while the 11 nm particles reduced the bacteria in the biofilm by 3.7±0.3 $\log_{10}$. Visually, the particles appeared to move across the bottom of the biofilm dish during the duration of the treatment. We attribute this physical movement to the mechanism behind the increase in bacterial reduction.

Though both of the applied magnetic fields reduced the bacteria within the biofilm, the AC magnetic field was the more effective treatment condition with 3.6±0.4 $\log_{10}$ and 3.9±0.3 $\log_{10}$ bacterial reductions for 8 nm and 11 nm particles, respectively. From the heating curves, the 11 nm particles have a higher heating efficiency than the 8 nm particles. Since no physical movement can occur at 191 kHz, this increased bacterial reduction is attributed to the hyperthermia-based increase in temperature
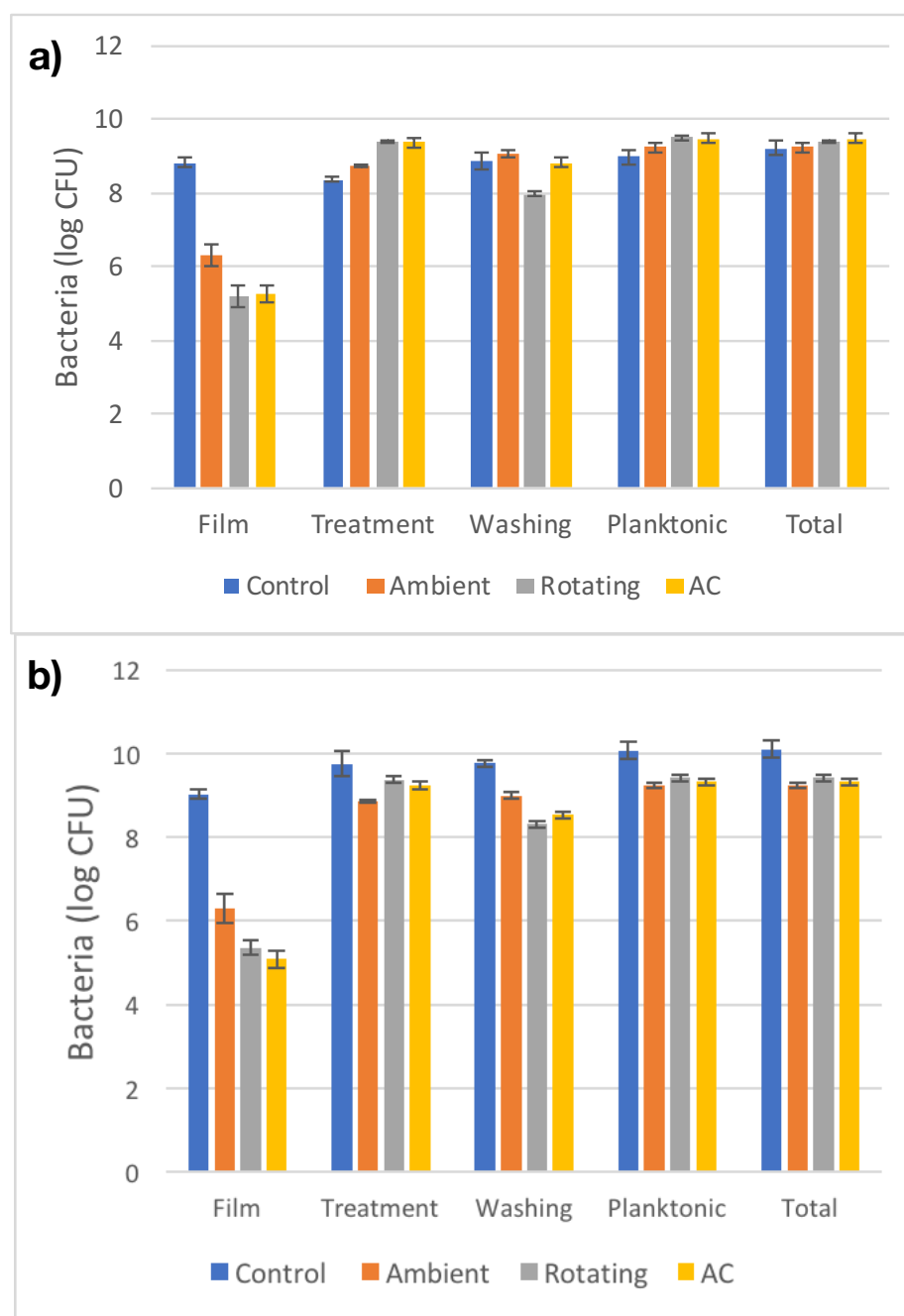
Figure 3.8: Biofilm test results for a) 8 nm and b) 11 nm spherical nanoparticles. The planktonic bacteria is the sum of the bacteria enumerated in the treatment and washing solutions; while the total bacteria is the sum of the biofilm and planktonic.

Table 3.2: Biofilm test results for 8 nm and 11 nm spherical nanoparticles. All numbers refer to $\log_{10}$ reduction of CFU. The planktonic bacteria is the sum of the bacteria enumerated in the treatment and washing solutions; while the total bacteria is the sum of the biofilm and planktonic.

Sample	Condition	Biofilm	Treatment sol.	Washing sol.	Planktonic	Total
8 nm	Ambient	2.5±0.5	-0.35±0.08	-0.2±0.4	-0.2±0.3	0.0±0.3
	Rotating field	3.6±0.4	-1.05±0.08	0.9±0.3	-0.5±0.2	-0.2±0.2
	AC field	3.6±0.4	-1.0±0.2	0.0±0.4	-0.5±0.3	-0.3±0.3
11 nm	Ambient	2.7±0.4	0.9±0.3	0.8±0.1	0.8±0.3	0.9±0.3
	Rotating field	3.7±0.3	0.4±0.4	1.5±0.1	0.6±0.3	0.7±0.3
	AC field	3.9±0.3	0.5±0.4	1.2±0.1	0.7±0.3	0.8±0.3

of the system.[75]

We must acknowledge that only examining the bacteria within the biofilms can be misleading since the bacterial reductions may be (erroneously) interpreted as killed bacteria. To obtain more insights, the planktonic bacteria in both treatment and washing solutions have also been enumerated so the total number of bacteria can be tracked. For the 8 nm spherical nanoparticles, treatment solutions of rotating and AC magnetic field samples contain 0.6±0.2 $\log_{10}$ and 0.7±0.3 $\log_{10}$ more bacteria than that of the ambient samples. This indicates that more bacteria are transferred to the treatment solutions when magnetic fields are used to manipulate the nanoparticles. However, when the bacteria in the washing solution is taken into account, both the planktonic and total amounts of bacteria are conserved (within uncertainties). Thus, while the amount of bacteria within the biofilm is reduced, there is no observable bacterial kill for samples treated with the 8 nm particles.
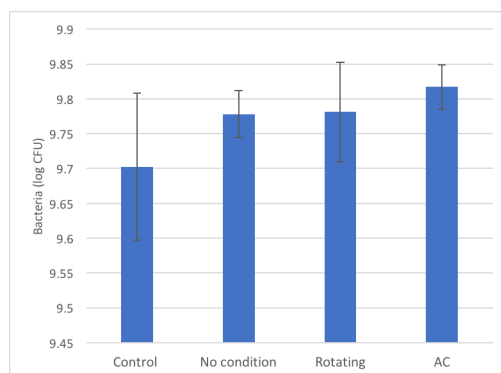
Figure 3.9: Bacterial test results for 11 nm spherical nanoparticles.

For the 11 nm particles there is also an increase in the amount of bacteria observed in the treatment solutions from the rotating and AC field samples compared to the ambient (0.5 ± 0.1 $\log_{10}$ and 0.4 ± 0.1 $\log_{10}$ more, respectively). The amount of bacteria in the washing solution of the treated samples seems to compensate for the differences in the treatment solutions, with the planktonic bacteria constant amongst all of the samples treated with 11 nm particles. Notably, the total number of bacteria was reduced by 0.8 ± 0.3 $\log_{10}$ for ambient and rotating field samples, and 0.9 ± 0.3 $\log_{10}$ for AC field samples. This means that the 11 nm particles successfully kill bacteria, while the 8 nm do not.

To isolate whether the 11 nm particles kill planktonic or sessile bacteria, the biofilm test was repeated with a planktonic solution substituted for the biofilm. From the results in Figure 3.9, there is no significant reduction between the control and any treatment using iron oxide particles. Instead, the results suggest a slight bacterial growth. This indicates that the bacterial kill must likely occur when the bacteria is trapped within the extracellular matrix of the biofilm.

While the matrix is typically beneficial to the bacteria, the electrostatic charges within the system suggest that the extracellular matrix facilitates the bacterial kill. From the zeta potential measurements, both the 8 nm and 11 nm particles have negative surface electric potentials, with the larger particles being slightly more positive by 12 ± 5 meV. Since the cell membrane of MRSA is primarily composed of negatively charged phospholipids, the bacteria have an effectively negative surface charge.[76][77] Minimal interaction with the negative nanoparticles is anticipated for planktonic bacteria due to Coulombic repulsion, in keeping with the planktonic results. However, the overall situation changes when the extracellular biofilm matrix is taken into account. This matrix is composed primarily of polysaccharides, though proteins and other molecules are also present.[67]

We propose that the negatively charged iron oxide particles are attracted to some component of the matrix with an effective positive charge. For both sizes of particles, this interaction causes damage to the biofilm matrix resulting in the release of bacteria even under ambient conditions. This attraction between the nanoparticles and the matrix serves an additional purpose though, because it brings the particles within the vicinity of the bacteria. Since the 11 nm particles have a weaker negative charge, they are less repulsed by the bacteria (increasing the possibility of contact). Upon contact, the nanoparticles can cause cell death by interfering with the electrostatic potential of the cell membrane or reactive oxidative species generation.[78][79]

Based on these results, we can design a system to optimize the effect of the nanoparticles on biofilms. For both sizes of spherical nanoparticles tested, the application of a high frequency AC magnetic field caused the greatest bacterial reduction

within the biofilms of the treatment conditions examined, with 11 nm particles having the best overall effect. Since this sample also has the greatest heating efficiency, we propose that increasing the SLP will improve the bacterial reduction. Because the hyperthermic effect is correlated to the overall anisotropy of the nanoparticles, there are two apparent ways of optimizing our system. The first method is to increase the magnetocrystalline anisotropy by replacing iron oxide with a doped ferrite (i.e. $CoFe_2O_4$)[80], however, these ferrites are not yet approved for medical applications. The second method is to increase the shape anisotropy by using anisotropic nanoparticles such as cubes or rods.[81][82] Since these non-spherical nanoparticles have unique demagnetization fields, they can be manipulated by magnetic field more easily than spherical nanoparticles. This means that the rotating field treatment could also be enhanced by the incorporation of different shapes.

3.5 Summary

Overall, we observe bacterial reduction in all MRSA biofilms treated with iron oxide nanoparticles. The greatest reduction occurred when a high frequency AC magnetic field was used to induce heating with 3.6 ± 0.4 $\log_{10}$ and 3.9 ± 0.3 $\log_{10}$ bacterial reductions for 8 nm and 11 nm particles respectively. When a rotating magnetic field was applied, the bacterial reduction was worse than ambient for 8 nm particles, but better for 11 nm particles due to aggregation in the 8 nm samples. Thus, we can manipulate the iron oxide nanoparticles to improve bacterial reduction in biofilms. When the planktonic bacteria is taken into account, the 8 nm particles do not kill bacteria while the 11 nm particles result in a $\sim$0.8 $\log_{10}$ kill. We attribute the increase in kill

to this system's more positive electric charge resulting in greater interaction between bacteria and nanoparticles. Following these results, we propose that different shaped nanoparticles can be used to optimize the effect of the nanoparticles on biofilms.

Chapter 4

Structure & magnetism temperature dependencies of Fe_3O_4 nanorods

4.1 Introduction

Magnetite nanorods have been chosen for their high degree of shape anisotropy and large demagnetization fields. However, changing from a system of small spheres to large rods has significant consequences. While the surface anisotropy is decreased, shape anisotropy must be considered. Additionally, though the spheres are single-domain Stoner-Wohlfarth particles, only the short axis of the nanorods falls within this limit. As such, the formation of magnetic domain walls and incoherent reversal modes are possible.

To add further complexity to the nanorod system, the Verwey transition is known to be affected by uniaxial strain.[45][46][48] For small spherical particles, the high degree of disorder and isotropic strain tends to eliminate the Verwey transition;[83] however, the effect of strain within anisotropic nanoparticles has not been fully studied.

In this chapter, wes do a full analysis of the temperature dependent characteristics of Fe_3O_4 nanorods.

4.2   Nanorod Synthesis

Hydrothermal nanorod synthesis works by creating an environment such that growth along one crystal plane is favoured. Initially, β-FeOOH nanorods were synthesized hydrothermally using a solution of ferric chloride-hexahydrate and urea in water as described by Zhihui Xu et al.[84] 9.4602 g of $FeCl_3 \cdot 6H_2O$ and 2.1000 g of urea were dissolved in 35 ml water. The entire solution was poured into a digestion vessel, 5 ml was removed, and the vessel was sealed and placed into a 125°C furnace for 4 hours.

The β-FeOOH nanorods were then reduced to Fe_3O_4 by suspending the particles in 50 ml oleylamine and heating to 210°C in an inert atmosphere under reflux conditions for 2 hours. The resulting particles were separated magnetically and washed extensively in hexane and acetone, ethanol, and methanol before air drying in a 60°C furnace.

4.3   Morphology and structure

TEM images (Figure 4.1) confirm the sample to be nanorods with lengths between 300 and 1100 nm and widths of 20-80 nm. Overall, the average aspect ratio is 13. Pitting is evident in the nanorods; this is likely a result of the reduction from β-FeOOH to Fe_3O_4. During this reaction, any chlorine impurities in the initial β-FeOOH will form HCl which subsequently dissolves the surrounding solid.

The room temperature XRD (Figure 4.2a) contains reflections consistent with a

spinel structure ($Fd\bar{3}m$) with lattice constant 8.3832(8) Å which implies the phase to be Fe$_3$O$_4$ rather than γ-Fe$_2$O$_3$.[19] From low temperature XRD, the sample undergoes a structural transition to a monoclinic phase consistent with a Verwey transition. Reitveld refinement of the pattern at 25 K with the $C2/c$ space group, as determined by Blasco et al.,[34] is most consistent with our data (see Figure 4.2b). The space group $Pmc2_1$ proposed by Iizumi et al. was considered; however, strain due to the nature of the crystallites has likely lowered the symmetry of the system.[33]

While the transition from a cubic to monoclinic phase is consistent with the Verwey transition in bulk magnetite, the refinement results suggest a far more extreme distortion to the crystal structure in the nanorods. In bulk magnetite, the monoclinic phase is the result of a lattice angle (β) shifting from 90° to 90.24°;[34] however, in the 25 K pattern, β shifts to 93.75±0.03°. Due to lower symmetry in the monoclinic phase, the unit cell of bulk Fe$_3$O$_4$ increases to $a_m = b_m = \sqrt{2}a_c$ and $c_m = 2a_c$ where a_c is the lattice constant in the cubic phase.[34] For the nanorods at 25 K, $a_m = 11.895 \pm 0.003$Å$= 1.419a_c$, $b_m = 11.854 \pm 0.002$Å$= 1.414a_c$, and
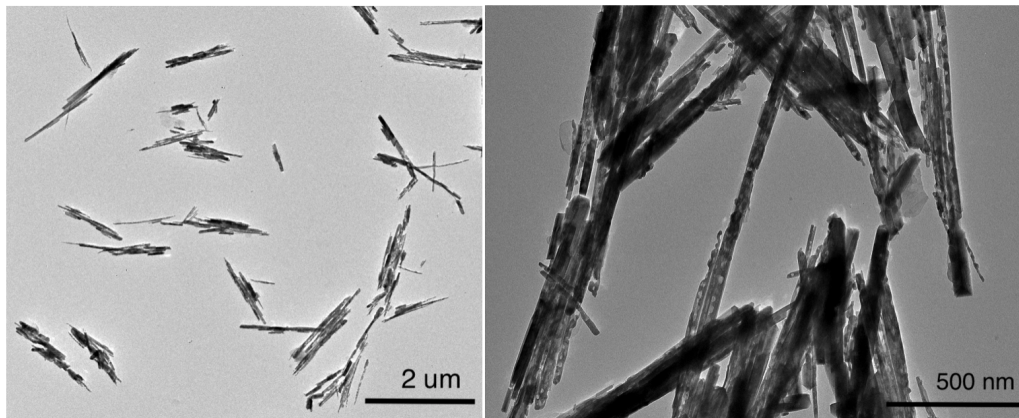
Figure 4.1: TEM images of Fe$_3$O$_4$ nanorods. High magnification image shows pitting on particles.
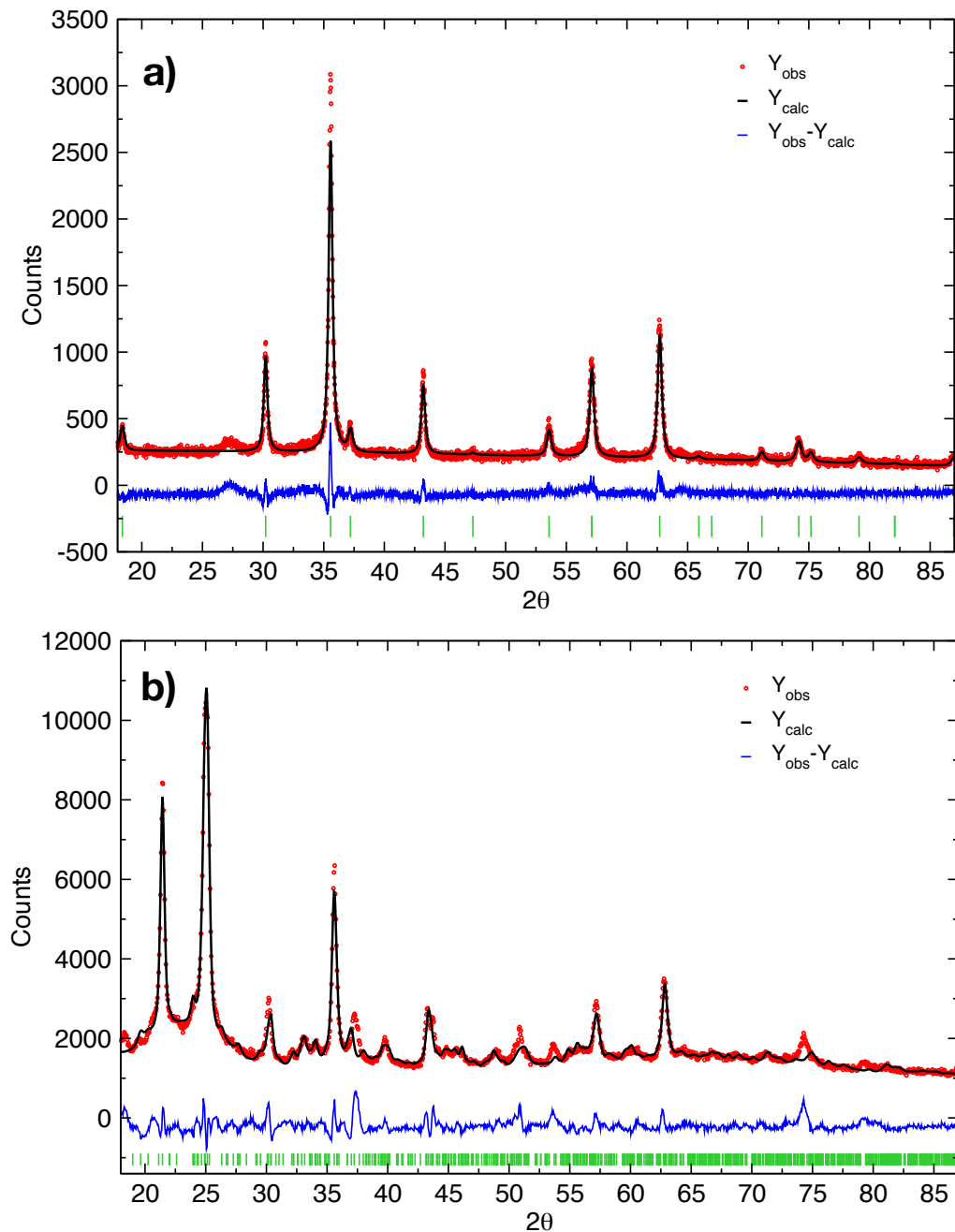
Figure 4.2: X-ray diffraction patterns of Fe$_3$O$_4$ nanorods at a) 300 K and b) 25 K. Red dots are data and black line indicates fit. The green Bragg markers index the a) $Fd\bar{3}m$ and b) $C2/c$ structures while the blue line is the residuals of the refinement.

$c_m = 14.45 \pm 0.02\text{Å} = 1.72a_c$. Thus a_m and b_m of the nanorods are in agreement with bulk predictions, while c_m is ~14% smaller, indicating compression along this axis.

The transition between the monoclinic and cubic phases was tracked over both warming and cooling cycles. Figure 4.3 shows the evolution of the diffraction pattern as the sample was warmed. At 225 K, the pattern is best fit with 23% monoclinic and 77% cubic phases and the lattice spacings of the monoclinic phase are the same within error as the 25 K pattern. As the temperature is increased, the monoclinic phase fraction decreases (as evidenced by the disappearance of the 22° and 25° diffraction peaks) until the pattern is fully cubic at 250 K. We conclude that the structural transition from a monoclinic to cubic phase occurs between 225 K and 250 K. When the nanorods were cooled from 300 K to 20 K, a more rapid transition from cubic to
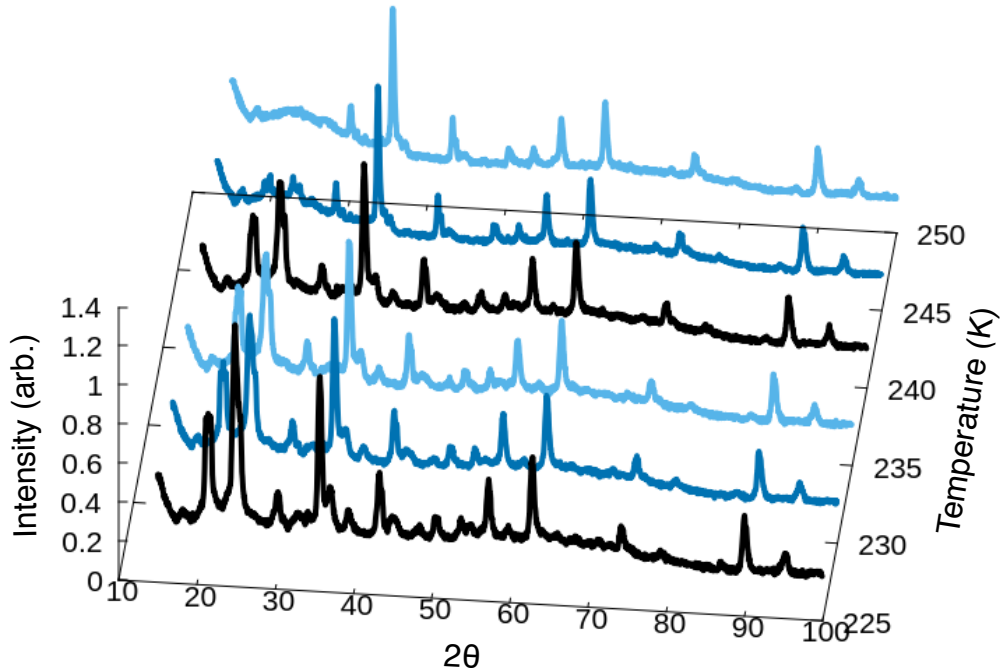
Figure 4.3: Temperature dependent x-ray diffraction patterns from 225 K to 250 K as the structure transitions from a monoclinic to a cubic state.

monoclinic structures occurs between 225 K and 215 K indicating structural hysteresis within the system.

4.4   Overall temperature dependent magnetism

The overall magnetic properties of the Fe$_3$O$_4$ nanorods were determined from magnetometry and susceptometry measurements; samples were dispersed in GE varnish to reduce interparticle interactions. Hysteresis loops were measured from 10 K to 400 K with ± 3 T field after cooling in zero field; a selection of these loops are presented in Figure 4.4.

Traditional hallmarks of T$_V$ are visible on the overall magnetism of the system. The coercive fields (H_C) obtained from hysteresis loops provides a measure of the magnetic anisotropy in a sample. From Figure 4.5, a sharp change in coercivity is observed at 100 K indicating a change in the overall anisotropy. Modelling of bulk
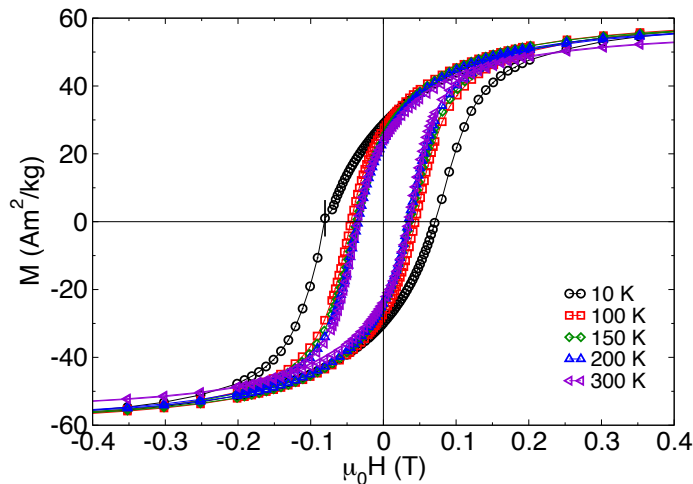
Figure 4.4: Low-field view of hysteresis loops of Fe$_3$O$_4$ nanorods.

magnetite by Muxworthy and Williams has shown that the limit of first cubic magnetocrystalline anisotropy constant (K_1) is 0 for temperatures approaching T$_V$.[85] Below the transition, an increase in overall anisotropy is typically interpreted as the result of the appearance of significant monoclinic anisotropy constants.

The thermoremanence of the system also reveals temperature dependent changes, as characterized via the squareness ratio (M_R/M_S) shown in Figure 4.6. Similar to the coercivity, the remanence of the system undergoes a sharp transition. This change in remanence between 100 K and 150 K speaks to changes to factors affecting domain wall motion.

From Bloch's Law describing coherent fluctuations of spinwaves, the temperature dependence of the magnetic saturation is reflected by $M_S(T) = M_S(0)(1 - BT^{3/2})$ where B is inversely proportional to the material's exchange interaction.[19] From
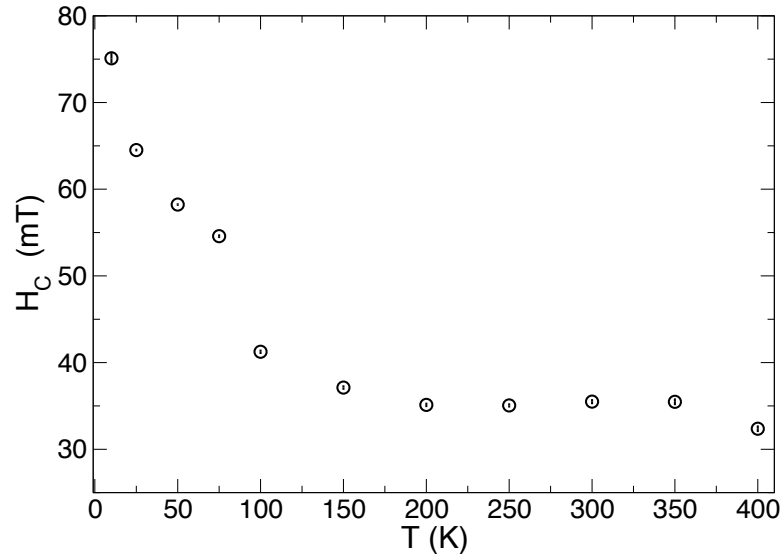
Figure 4.5: Coercive field (H_C) as a function of temperature. A change in behaviour is evident between 100 and 150 K consistent with the structural change observed in XRD.
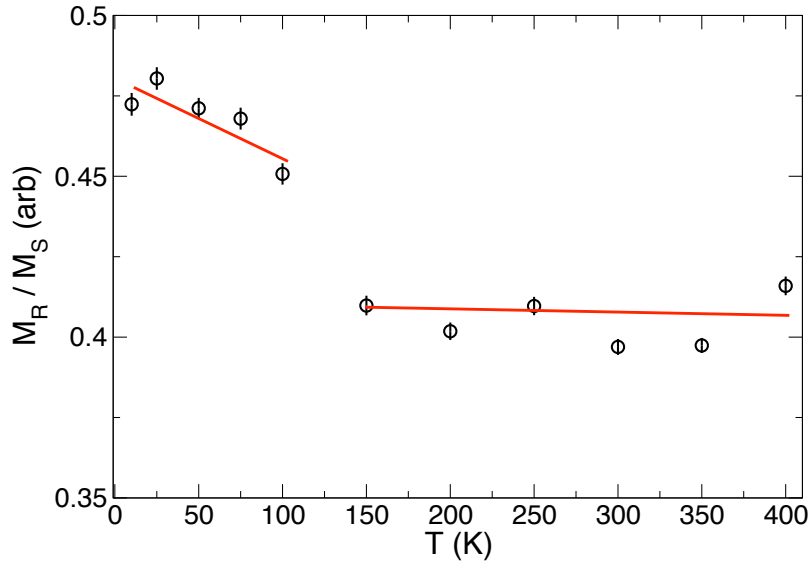
Figure 4.6: Squareness ratio as a function of temperature. A change in slope is evident between 75 K and 100 K indicating a change in anisotropy. Linear regimes are marked in red to guide the eye.
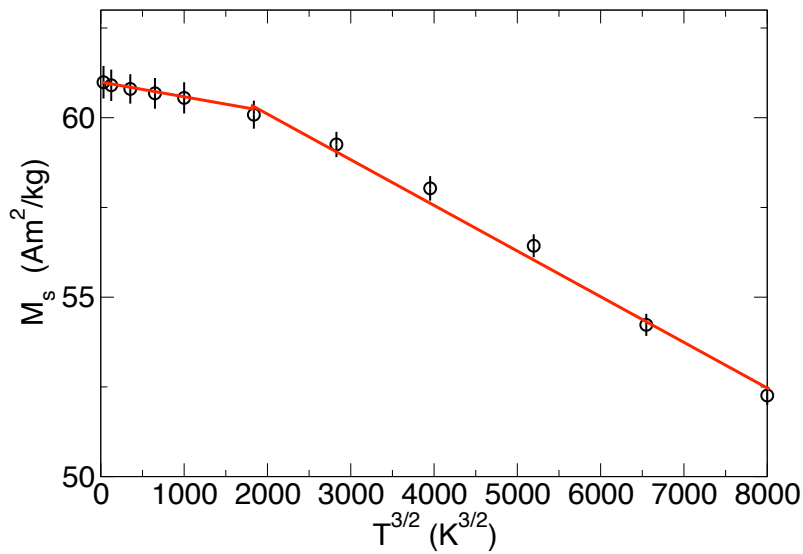
Figure 4.7: Magnetic saturation as a function of T$^{3/2}$. Linear regimes are marked in red to guide the eye; the transition between two regimes occurs at 150 K.

Figure 4.7, a change in the exchange interactions occurs at 150 K as evidenced by the change in slope. This is the same temperature where the thermoremanence sharply decreased; both of these behaviours are consistent with a structural change. While from XRD the system transitions from a monoclinic to a cubic phase from 225 K to 250 K, the temperature dependent behaviour observed the overall magnetism is the result of changes in the microstructure.

4.5   Links between microstructural changes, Fe coordination and atomic magnetism

Since Mössbauer spectroscopy probes the local environment of ^{57}Fe, it is an ideal tool for tracking changes from variations in the microstructure. In particular, the isomer shift (δ) provides information about the local electronic environment, specifically the interaction between the nucleus and the s-orbitals. Due to shielding effects, the s-orbital density is affected by the d-orbitals; this allows the isomer shift to reflect oxidation state and bonding environment. The magnetic hyperfine field (B_{hf}) describes the magnetic environment at the nucleus where the dominant contribution is typically the Fermi contact term (due to unpaired valence electrons), though the orbital moment of these valence electrons and the non-spherical distribution of electron spin density also play a role. Because the Verwey transition is known to affect both the electronic and magnetic properties of Fe_3O_4, changes in δ and B_{hf} are evidence of this transition.

Initially, the 10 K Mössbauer spectrum was fit with three sextets corresponding to the tetrahedral (T_d) A site's Fe^{3+} and octahedral (O_h) B site's Fe^{2+} and Fe^{3+} (see

Fig. 4.8) predicted by Verwey's charge ordering model.[86] The tetrahedral A site accounts for 40% of the absorption with hyperfine parameters δ=0.441±0.006 mm/s, Γ=0.25±0.02 mm/s and B_{hf}=51.34±0.07 T. Site B1 relates to octahedral Fe^{2+} with δ=0.56±0.01 mm/s, Γ=0.44±0.04 mm/s and B_{hf}=48.3±0.2 T, while site B2 corresponds to octahedral Fe^{3+} with δ=0.507±0.007 mm/s, Γ=0.21±0.03 mm/s and B_{hf}=53.54±0.07 T. The oxidation state was determined from the hyperfine fields since the theoretical limit of Fe^{2+} is lower than that of Fe^{3+}.[56]

The B1 and B2 components account for 36% and 24% of the fitted absorption, respectively. This means that the relative areas of the fit do not match Verwey's model of three equivalent components resulting from A-site Fe^{3+}, and B-site Fe^{2+} and Fe^{3+}. Further analysis of the fit spectrum reveals that there is absorption along the inner edge of line 2 that is not accounted for in the three component fit. Since the line width of B1 is significantly larger than the other components, and the relative absorption of B2 suggests a deficiency in B-site Fe^{3+} ions, we revised the fit using
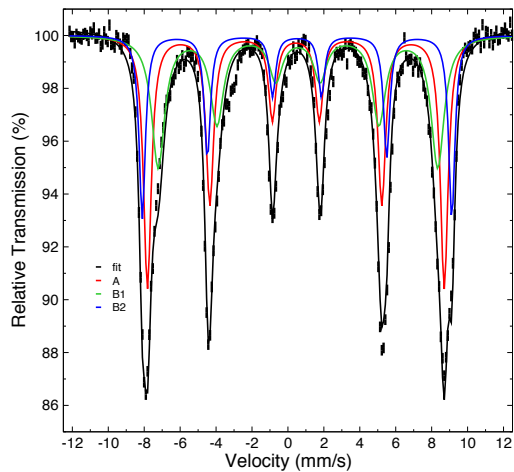
Figure 4.8: Mössbauer spectra at 10K with three component fit. Components A, B1 and B2 represent tetrahedral Fe^{3+}, and octahedral Fe^{2+} and Fe^{3+} respectively.

four components with the additional sextet (B3) corresponding to octahedral Fe^{3+}.

In this revised four component fit (Fig. 4.9), the relative areas of the sites A:B1:B2:B3 are 8:8:5:3; which corresponds to the expected 1 to 2 ratio of A-site to B-site ions for stoichiometric Fe$_3$O$_4$. The hyperfine parameters of the four sextet fit are summarized in Table 4.1, with no significant changes to the A site. From the isomer shifts of 0.517±0.009 mm/s and 0.517±0.007 mm/s respectively, the B1 and B2 components are located in identical electronic environments implying a strong interaction. Again, the oxidation states of these sites can be distinguished by their hyperfine fields of 49.39±0.07 T and 52.71±0.05 T as Fe^{2+} for B1 and Fe^{3+} for B2. Thus we can conclude that all of the octahedral Fe^{2+} interacts with the majority of the octahedral Fe^{3+}.

This interaction is consistent with the trimeron picture where all of the Fe^{2+} share t$_{2g}$ electrons with acceptor ions and all but one acceptor is Fe^{3+}.[39] Since site B3 has a distinctly different isomer shift from the other B sites (δ=0.79±0.04 mm/s), these Fe^{3+}
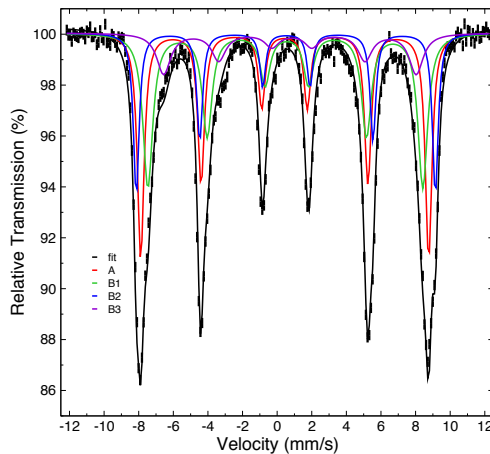
Figure 4.9: Mössbauer spectra at 10K with 4 sextet fit. Site ratios of A:B1:B2:B3 are 8:8:5:3. Hyperfine parameters are tabulated in Table 4.1

Table 4.1: Hyperfine parameters of 10 K Mössbauer spectra of Fe_3O_4 nanorods.

Site	δ (mm/s)	Γ (mm/s)	B_{hf} (T)	Area (%)
A	0.432±0.004	0.23±0.01	51.70±0.04	33.4
B1	0.517±0.009	0.20±0.02	49.39±0.07	33.3
B2	0.517±0.007	0.34±0.02	52.71±0.05	20.8
B3	0.79±0.04	0.49±0.07	45.3±0.3	12.5

are not bound to trimerons; however, its large line width (Γ=0.49±0.07 mm/s) speaks to a large degree of disorder. In a perfect low temperature Fe_3O_4 single crystal, only two of the eight Fe^{3+} ions do not participate in a trimeron formation;[39] however, we can attribute the additional B3 absorption to the weakening of trimerons from increased crystal strain.[47] Effectively, the B-site is split into eight central Fe^{2+}-like ions, five Fe^{3+}-like acceptor ions and three Fe^{3+} ions.

By tracking the temperature evolution of the hyperfine parameters, we see that the A site is relatively constant from 10 to 300 K. The decrease in both δ and B_{hf} with increasing temperature may be attributed to a second order Doppler shift. In contrast, the B site reveal a dynamic microstructure, with the components undergoing subtle shifts in the low temperature regime (<150 K) and a significant transformation at 150 K. The subtle changes are most evident in the isomer shifts of the interacting B1 and B2 sites in Figure 4.10, where these parameters diverge first at 25 K and again at 100 K. Because the isomer shift speaks to electronic environment and valence state, variations in δ suggests changes to the coordination of the trimerons. At both temperatures, a simultaneous decrease in δ of B3 is observed which indicates that all B site components are affected by trimeron dynamics.

At 150 K, the B sites undergo a drastic transformation as the three low temperature sextets are replaced by one sextet (B1′) and a broad singlet (B2′). At 300 K (see Figure 4.11), the measured isomer shifts of the A and B1′ sextets are 0.350±0.007 and 0.66±0.02 mm/s respectively which matches well with literature values of 0.32 mm/s
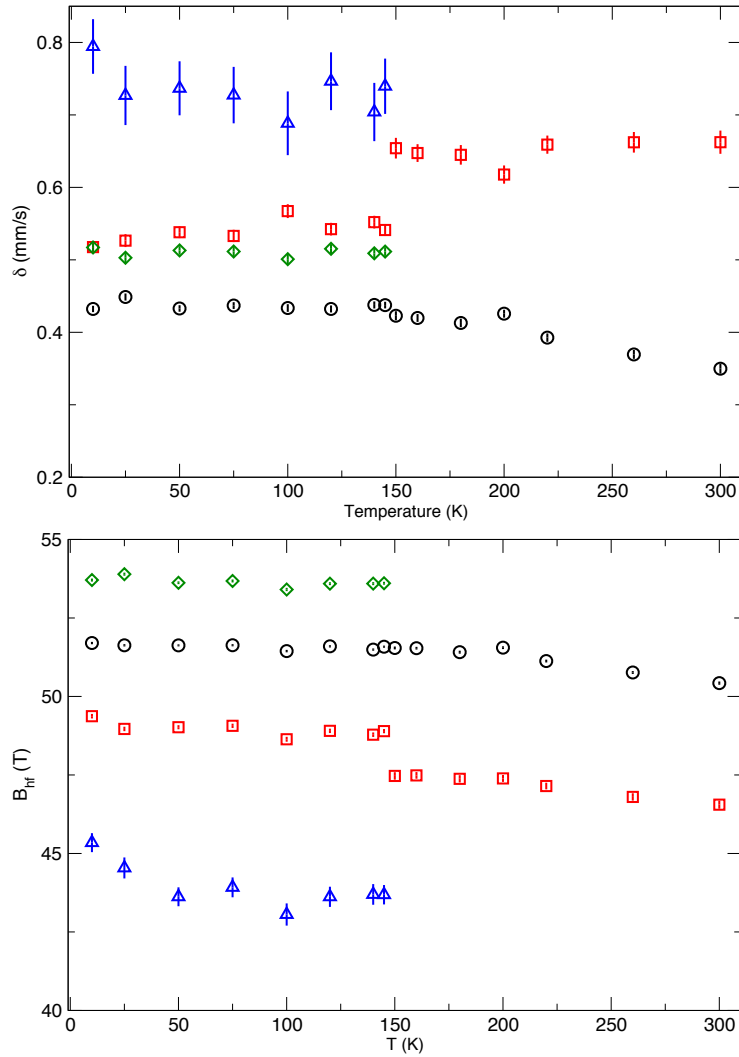
Figure 4.10: Isomer shift (δ, top) and hyperfine field (B_{hf}, bottom) obtained from temperature dependent Mössbauer spectra. Black circles are component A and red squares are component B1/B1′. Below 150 K, green diamonds are component B2 and blue triangles are component B3. Hyperfine parameters for broad sextet component (B2′) not depicted as both δ and B_{hf} are 0.
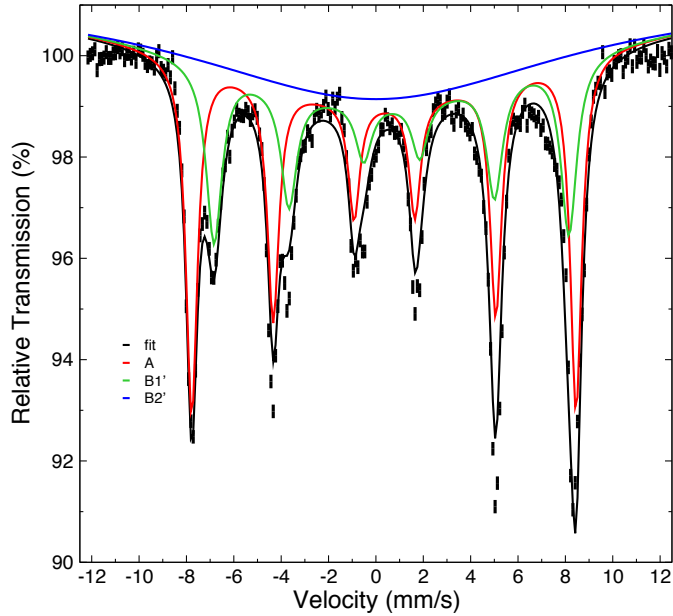
Figure 4.11: Mössbauer spectra at 300K with two sextet fit.

and 0.66 mm/s reported for 31 nm Fe$_3$O$_4$ nanoparticles.[87] Similarly, the hyperfine fields of 50.42±0.05 T and 46.6±0.1 T correspond to the reported values of 49.1 T and 45.7 T.[87] This fit reflects the dissolution of the trimerons and recovery of the Fe$^{2.5+}$ octahedral sites expected in the cubic phase at 150 K.[72]

While the Mössbauer spectra speak to the individual Fe sites, the measured relative absorption (f-factor) of a Mössbauer spectrum provides information about changes in bonding environment about the ^{57}Fe ions through changes in the phonon modes. Essentially, the f-factor provides information about the lattice. From Fig. 4.12, measurements[1] show a change in behaviour at 150 K consistent with the structural change and associated freezing of phonon modes described by Senn et al.[88] While

---

[1] Additional Mössbauer spectra with velocities ±13 mm/s were used to calculate f-factor in order to ensure a more accurate baseline.
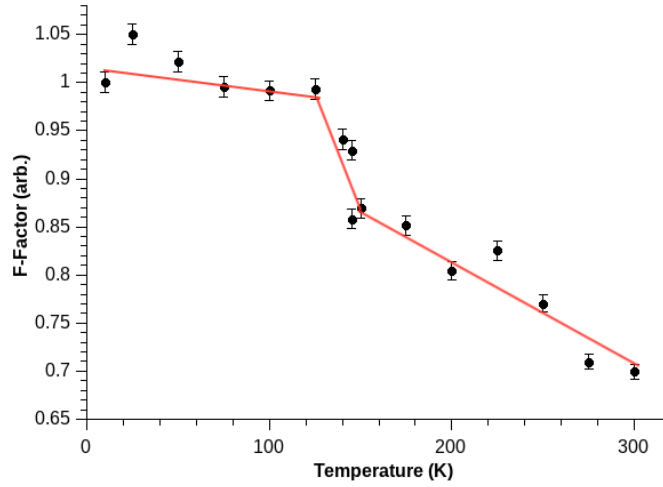
Figure 4.12: Temperature dependence of f-factor. A structural transition is evidenced by the jump at 150 K.

this temperature does not match the transition between monoclinic and cubic space-groups observed via XRD, it does correspond to the dissolution of trimerons observed in the fit Mössbauer spectra as well as the changes in behaviour of both M_R/M_S and $M_S(T^{3/2})$. This suggests that the transition from a monoclinic to a cubic phase is a multi-step process, where changes to the local coordination of Fe B-site ions cause a softening of phonon modes, then an overall structural change occurs upon further warming.

Regardless of whether we consider our effective T_V to be the changes in microstructure/local coordination or overall structure, these temperatures are incongruous with the expected Verwey temperature (T_V) of ~120 K in bulk magnetite.[32] We know from XRD refinement that the sample exhibits considerable strain. High pressure measurements of powder Fe_3O_4 have determined that T_V is inversely related to applied pressure [43][44]; however the applied pressure for these experiments was isotropic. In the nanorods samples, strain is likely favour certain crystal planes

which may cause the transition temperature to increase. Such an increase has been previously observed in strained Fe_3O_4 thin films [45][46] as well as single crystals.[48]

4.6   Elemental magnetism

To identify further information on the elemental coordination of the Fe sites and gain insights into the O_2 bonding, x-ray absorption spectroscopy (XAS) was collected over the Fe L-edge (700-740 eV) and O K-edge (510-560 eV). The Fe XAS spectra at 10 K is consistent with that of a spinel iron oxide.[89] From the simulation in Figure 4.13,[64] with Fe^{3+} in a tetrahedral coordination (T_d), and both Fe^{2+} and Fe^{3+} in an octahedral coordination (O_h), the relative site areas of the Fe L_3-edge match well with the 10 K Mössbauer spectrum fit. Minor differences in the XAS simulation may
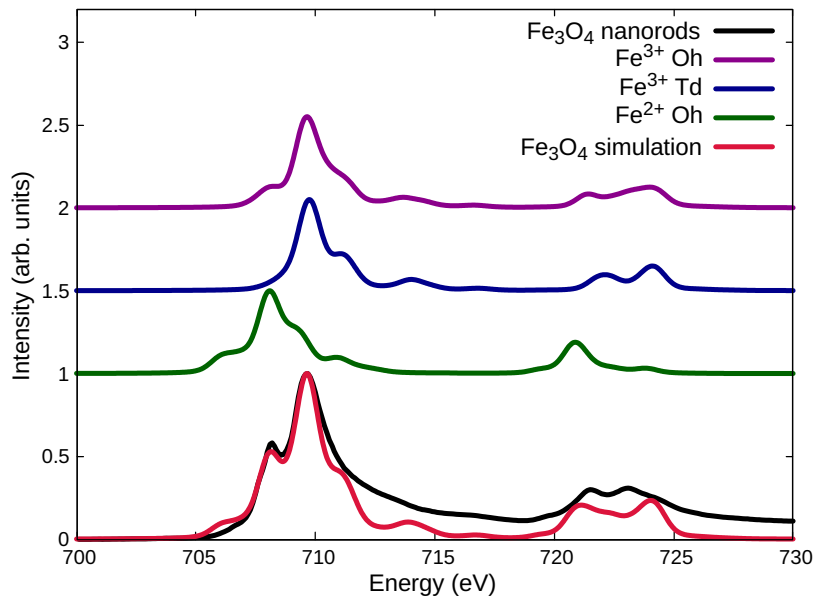
Figure 4.13: Fe L-edge XAS spectra and simulation at 10K. The experimental data is black, while the simulated spectra is red. The simulated spectra for the Fe^{3+} O_h (purple), Fe^{3+} T_d (blue), and Fe^{2+} O_h (green) also shown. The simulated spectra is the sum of 34% Fe^{3+} O_h, 32% Fe^{3+} T_d, and 34% Fe^{2+} O_h.
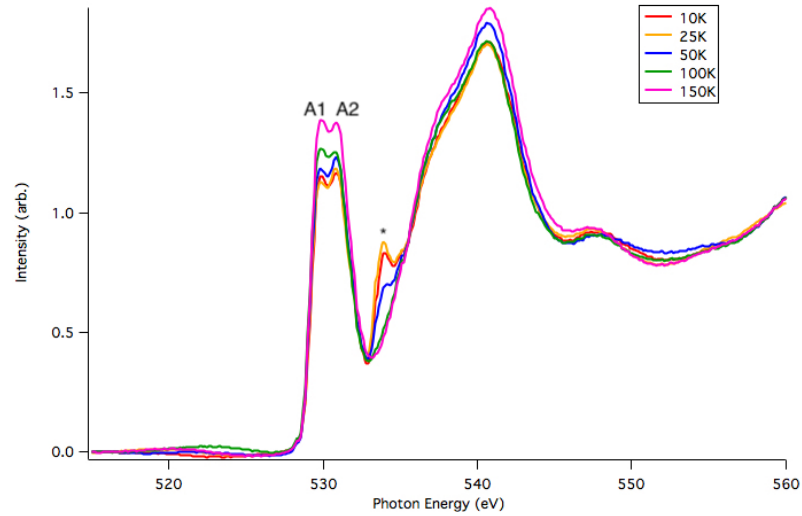
Figure 4.14: O K-edge XAS spectra. The prepeak is split into components A1 and A2 which approximate the t$_{2g}$ and e$_g$ electrons respectively. The (*) marks the trapped O$_2$ from the carbon tape; this peak decreases with temperature as the O$_2$ melts.[90]

be attributed to charge sharing and distortion caused by the formation of trimerons in the B sites below T$_V$. Since the octahedral Fe^{2+} and Fe^{3+} interact to form trimerons, tracking these constituents would provide insight into the temperature dependence of the quasiparticles. Due to the overlap between the Fe^{3+} ions in the XAS spectra, it is difficult to isolate the contributions of the tetrahedral Fe^{3+} from the octahedral.

However, because the sharing of t$_{2g}$ electrons is a signature of trimeron formation, the O K-edge XAS spectra can also be used to examine the temperature evolution of trimerons. The splitting of the prepeak into two components (labeled A1 and A2 in Fig. 4.14) has been established as a window into the nature of the t$_{2g}$ and e$_g$ symmetry bands in d^5 ions [91][92]. Since the electronic interactions of d^6 ions result in a broad unsplit pre-peak, the ratio of the A1 to A2 peaks gives insight into the t$_{2g}$ to e$_g$ proportion for only the Fe^{3+} sites. Because the tetrahedral Fe^{3+} is not involved directly with the formation of trimerons, changes in the observed peak ratio can be

attributed to the octahedral Fe^{3+}. From our understanding of trimerons, the central octahedral Fe^{2+} generally shares t$_{2g}$ electrons with the acceptor octahedral Fe^{3+}; thus, these ions transition from a d^5 to a more d^6-like state. This change causes the splitting of the measured O K-edge pre-preak to be reduced and an apparent decrease in the t$_{2g}$ to e$_g$ ratio. From Fig. 4.15, t$_{2g}$ electrons are the minority species below 100 K; this is consistent with the sharing of electrons between octahedral Fe^{2+} and Fe^{3+} in the trimeron picture. The minimum value at 25 K indicates the maximum electron sharing which we interpret as the strongest trimeron state. At 100 K, t$_{2g}$ electrons become the majority species indicating a reduction in electron sharing and weakening of trimerons.

X-ray magnetic circular dichroism (XMCD) was collected over the Fe L-edge (Fig. 4.16), to determine the elemental magnetism in the system. In a ferrimagnetic system, the A and B sites are coupled antiferromagnetically causing the XMCD spectra to be split accordingly; thus decoupling the signals from the tetrahedral and octahedral Fe^{3+}. Since each site corresponds to an individual L$_3$ XMCD peak, we are
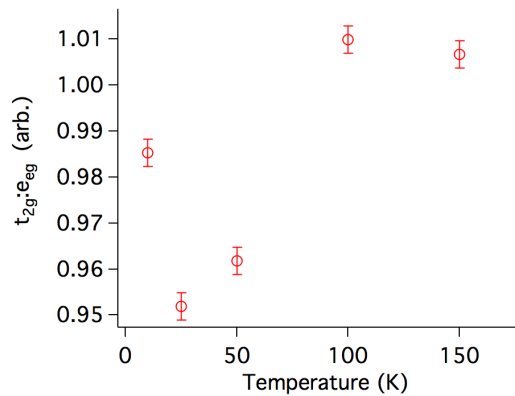
Figure 4.15: Ratio of t$_{2g}$:e$_g$ electrons as a function of temperature. Ratio was determined by relative amplitudes of A1 and A2 peaks in O K-edge XAS spectra.
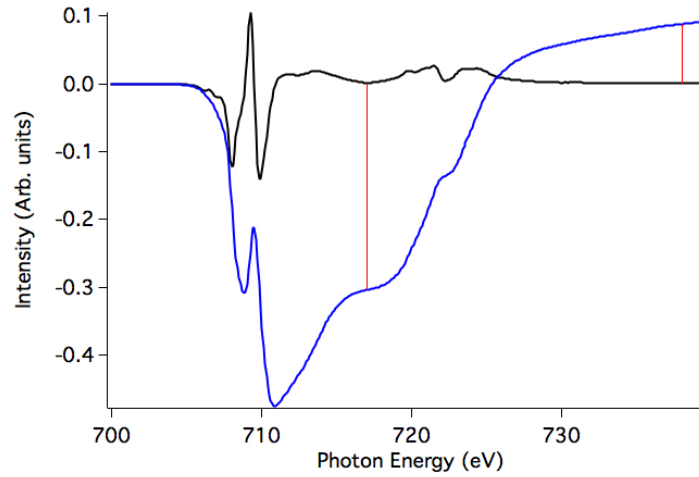
Figure 4.16: Fe L-edge XMDC spectra and integrated area at 10K. Lines at 717 eV and 738 eV mark p and q used in sum rules analysis.

able to track how the magnetism of individual sites changes as a function of temperature. As seen in Fig. 4.17, the magnetic signal of both Fe^{2+} O_h and Fe^{3+} T_d decrease linearly with increasing temperature up to 150 K. By contrast, the Fe^{3+} O_h site's magnetic intensity reaches a maximum at 25 K; this corresponds to the minimum t_{2g} to e_g value indicating the strongest interaction between trimeron constituents.

Because the orbital moment (m_l) and spin moment (m_s) contribute differently to
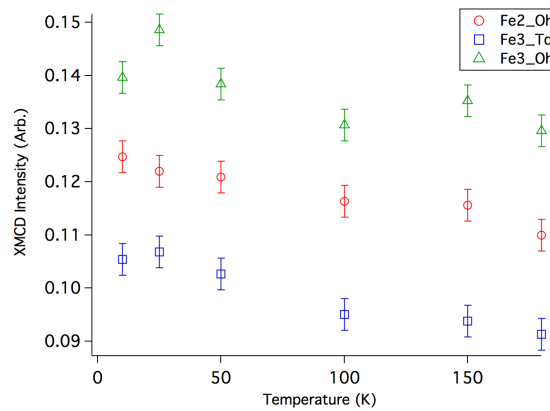
Figure 4.17: Absolute values of XMCD site amplitudes as a function of temperature.
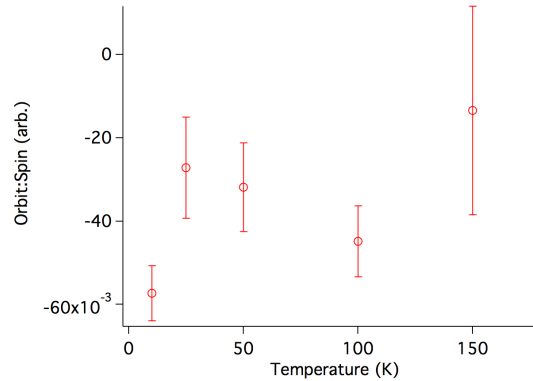
Figure 4.18: Orbit to spin ratio of Fe$_3$O$_4$ nanorods.

the L$_2$ and L$_3$ edges, the XMCD spectra can also be analyzed using sum rules analysis to determine the ratio m_l/m_s where $m_l/m_s = 2q/(9p-6q)$.[63] The parameters p and q are the integrated XMDC intensities over the L$_3$ and combined L$_2$ and L$_3$ edges respectively (see Fig. 4.16). From Fig. 4.18, the magnitude of the orbit to spin ratio undergoes a local minima at 25 K; this means that the system's net orbital moment is minimized when the trimeron electron sharing is maximized. Since bulk Fe$_3$O$_4$ has no orbital moment, this is truly nanoscale behaviour.

4.7   Discussion

We have utilized a number of techniques to obtain a complete picture of how Fe$_3$O$_4$ nanorods undergo a Verwey transition. From x-ray diffraction, the sample is cubic at room temperature and a highly distorted monoclinic phase at 25 K, indicating a highly strained system. From Mössbauer spectroscopy, we have confirmed the existence of trimerons in the low temperature (< 150 K) phase creating a foundation for our analysis.

By focusing on the B-site components that form these quasiparticles, a dynamic system is revealed. At 25 K, the trimerons are most strongly bound as evidenced by the minimum t_{2g} to e_g ratio. From the corresponding increase in the f-factor, the maximum trimeron interaction leads to a stiffening of the lattice. This effect is consistent with the increase in the squareness ratio, since a change in phonon modes would affect the thermomagnetic remanence.

At 100 K, the relative increase in t_{2g} electrons is clear evidence of the electronic decoupling of the trimerons suggested by the divergence of the isomer shifts of the two trimeron constituents (denotes B1 and B2). This change in the electronic bonding corresponds to a sharp decrease in the coercivity indicating that the overall anisotropy is affected by the reduction of charge sharing.

While the trimeron electron sharing decreases at 100 K, the majority of these quasiparticles dissolve at 150 K. Similar to what was observed at 25 K when the trimeron bonding was maximized, the dissolution of trimerons leads to a relaxation in the lattice and a sharp decrease in both f-factor and the magnetic remanence. Unsurprisingly, the trimeron dissolution also corresponds to a change in the exchange as evidenced by the change in behaviour of $M_S(T^{3/2})$.

Above 150 K, there are no significant changes in the electronic configuration affected by microstructural changes observed via the Mössbauer fit parameters. However, at 225 K, when the systems begins to recover the cubic phase, there is a slight increase in lattice stiffness as evidenced by the increases in f-factor, and M_R/M_S.

4.8   Summary

In summary, magnetite nanorods have a high degree of intrinsic strain. While low temperature measurements reveal a clear Verwey transition complete with the formation of trimerons, tracking the transition through warming reveals clear differences between our system and bulk Fe$_3$O$_4$. Rather than a unique transition temperature, the nanorods undergo a multistage transition; additionally, our measurements suggest the persistence of trimerons beyond the monoclinic phase. Because trimerons have been coupled to the change in electronic properties, these nanoparticles could be interesting from the perspective of electronics applications.

Chapter 5

Shape effects of Fe_3O_4 nanorod magnetism

Thus far, we have examined how the structure and magnetism of Fe_3O_4 nanorods change as a function of temperature. Because of the coupling between shape and strain, the effect of shape has been implicit to the discussion in Chapter 4. However, nanorods have both a large demagnetizing factor and shape anisotropy that affect their magnetic behaviour. In this chapter, the angular dependence of the overall magnetism will be analyzed to determine the effect of shape on the magnetic reversal mode.

5.1 Angular dependence of overall magnetism

From the Stoner-Wohlfarth theory, the shape of a hysteresis loop depends on the angle (α) between the applied field and the magnetic easy axis (see Equation 1.9 and Figure 1.5). Thus far, the Fe_3O_4 nanorods have been analyzed in a random dispersion. To examine the angular dependence of the overall magnetism, measurements were also done on dispersions aligned using an external magnetic field. Samples were prepared
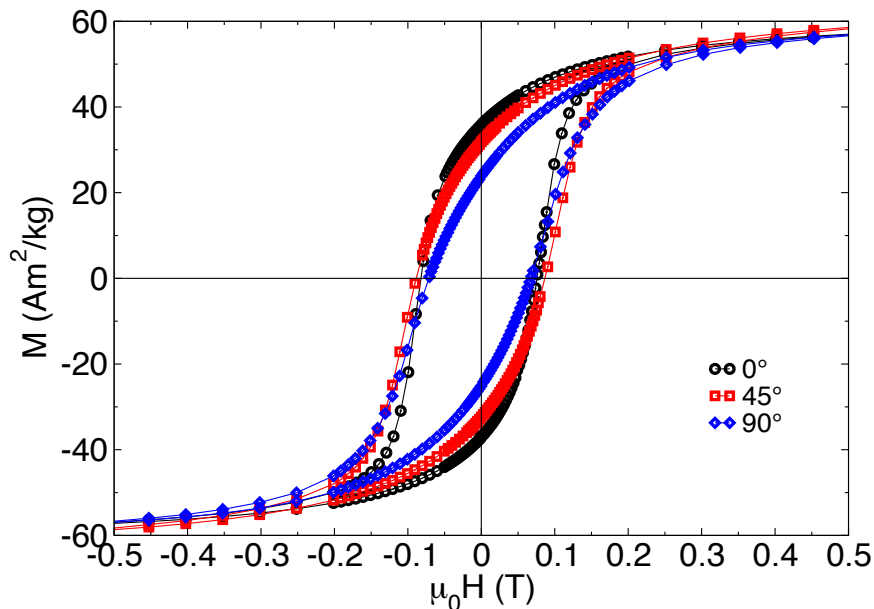
Figure 5.1: Low field region of 10 K hysteresis loops of Fe_3O_4 nanorods for $\alpha = 0°$ (black circles), $\alpha = 45°$ (red squares), and $\alpha = 90°$ (blue diamonds) where α is the angle between the applied field and the magnetic easy axis.

using the same concentration of nanorods in GE varnish as for the random dispersion to keep the keep the interparticle interactions similar. The nanorod suspension was sonicated, then dropped on a glass slide within a 2 T magnetic field. The sample was allowed to dry, then mounted for magnetometry such that the easy axis was parallel ($\alpha = 0°$), perpendicular ($\alpha = 90°$), and at 45° ($\alpha = 45°$) to the applied field, $\mu_0 H$.[1]

The 10 K hysteresis loops of these three alignments are shown in Figure 5.1. As predicted, there is an angular dependence to loop shape; however, it does not match the Stoner-Wohlfarth model since the $\alpha = 90°$ measurement has a non-zero coercivity. The simplest explanation is that there are some nanorods that are not fully aligned in the system resulting in a convolution between the desired angle and the

---

[1]Each alignment was mounted separately. The mass of particles within each sample was determined by normalizing to the magnetic saturation at 300 K to that of a powder sample.

random dispersion examined in Chapter 4. But since a 2 T field was used to align the nanorods, this is unlikely to be the case. Additionally, the Stoner-Wohlfarth model is built around the assumption of a coherent reversal mode. Since the diameter for these Fe_3O_4 nanorods is 20-80 nm, a significant fraction of the sample exceeds the critical curling diameter of $\sim$39 nm,[28] predicting that curling will occur. Due to the complexity of this system, with a size distribution, and transitions in both overall structure and microstructure, our examination of the angular dependence overall magnetism will be largely qualitative.

As predicted from the Stoner-Wohlfarth model, the squareness ratio (M_R/M_S) decreases with increasing angle (see Figure 5.2). Below 150 K, there is the same temperature dependence for each of the three angles measured; however, there are clear differences above 150 K. Since the squareness ratio is a reflection of factors affecting
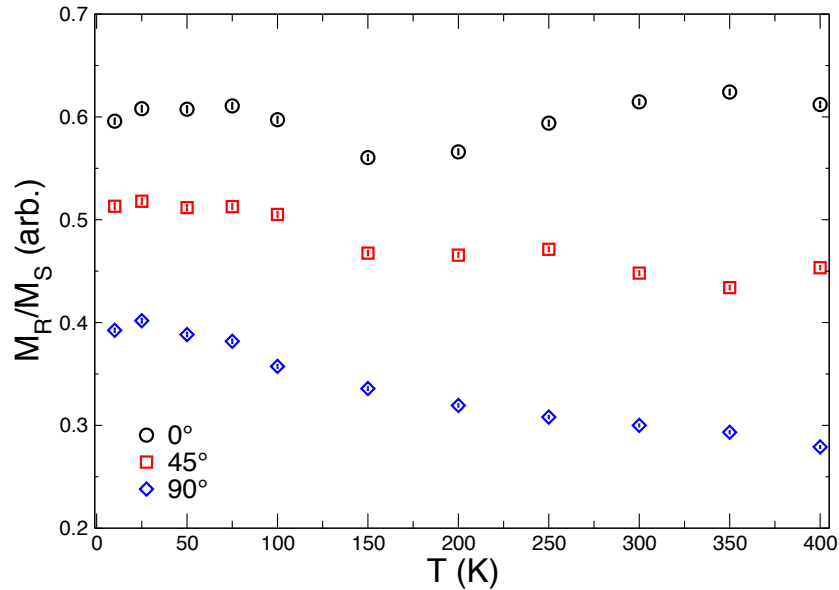
Figure 5.2: Temperature dependence of squareness ratio of Fe_3O_4 nanorods for $\alpha = 0°$ (black circles), $\alpha = 45°$ (red squares), and $\alpha = 90°$ (blue diamonds).

domain wall motion, we conclude that below 150 K the three orientations reverse similarly. From our Mössbauer spectroscopy results, this corresponds to the temperature region where the B-sites form trimerons. The interactions between trimeron components could prevent curling from occuring.

Above 150 K, M_R/M_S of the perpendicularly aligned ($\alpha = 0°$) nanorods decreases monotonically as a function of temperature while that of the parallel sample increases. These results are consistent with the reversal observed by Paulus et al.[93] on Co nanowires with 25 nm diameter, but differ from the behaviour of Fe and Ni nanowires. Because the change in behaviour has been attributed to strain between the hcp and fcc Co in the Co nanowires causing competition between magnetocrystalline and shape anisotropies, it is sensible that our strained Fe_3O_4 nanorods have a similar trend.

The Co nanowires at $\alpha = 0°$ have a 12% increase in squareness ratio from 150 K to 290 K,[93] while same alignment of our Fe_3O_4 nanorods presented a 10% increase over the same range. Differences in the values can be attributed to the different aspect ratios, however the squareness ratio suggests that the Fe_3O_4 nanorod domains reverse via curling for at least $\alpha = 0°$. Meanwhile, the monotonic decreases in the squareness ratios for both Co nanowires and our Fe_3O_4 nanorods aligned with $\alpha = 90°$ are consistent with coherent rotation. For $\alpha = 45°$ of the Fe_3O_4 nanorods, the squareness ratio undergoes an inflection point at 250 K —the same temperature as the transition between the monoclinic and cubic phases. We associate this change to a change in the magnetic easy axis due to the structural transition. Since M_R/M_S of $\alpha = 45°$ decreases slightly above 250 K (a 4% decrease from 250 K to 400 K), this angle seems to be close to the transition between reversal modes.

This is supported by our measurement of the coercive field (H_C) as a function of both temperature and angle, shown in Figure 5.3. From the Stoner-Wohlfarth model, H_C should decrease as the angle between the easy axis and applied field increases; however, for the nanorods, the largest H_C was measured at $\alpha = 45°$. The coercive field is proportional to the amount of energy required to reverse the magnetization. When the applied magnetic field is along the easy axis, the large demagnetization factor makes curling more energetically favourable than coherent reversal. As the angle between the applied field and easy axis is increased, the demagnetizing field decreases, until the energy required to initiate a curling reversal mode exceeds that required to overcome the demagnetization field.[28] At this angle, the maximum coercive field will occur and coherent reversal becomes the preferred mode.[94][95]

For the Fe₃O₄ nanorods, H_C at $\alpha = 45°$ is $\sim$22% larger than H_C at $\alpha = 0°$
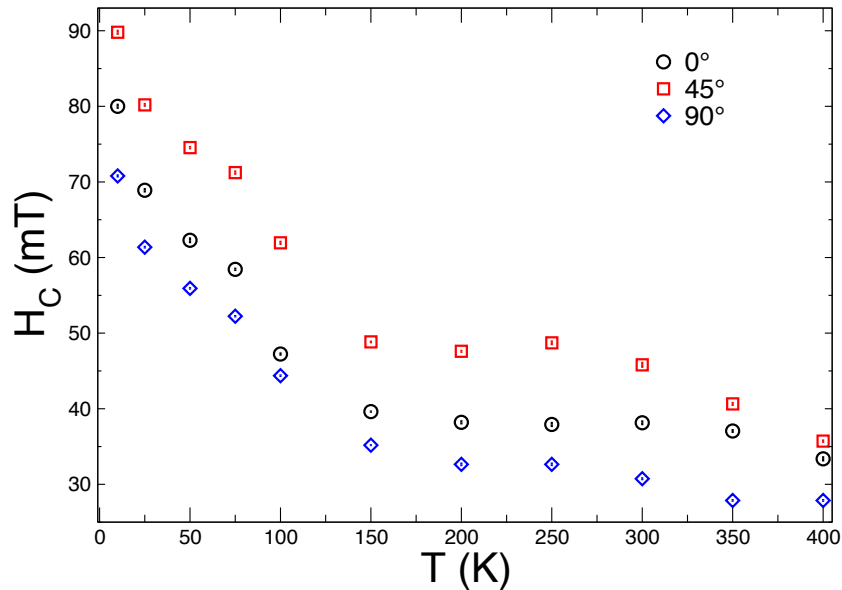
Figure 5.3: Temperature dependence of coercive field of Fe₃O₄ nanorods for $\alpha = 0°$ (black circles), $\alpha = 45°$ (red squares), and $\alpha = 90°$ (blue diamonds).

below 250 K. This is in line with the values Goolaup et al.[94] have reported for Ni$_{80}$Fe$_{20}$ nanowire arrays, where the maximum coercivity (before coherent reversal) ranges from 25% to 150% (depending on wire thickness) higher than that at $\alpha = 0°$. We attribute the lower percent increase in our nanorods to the disorder within our system because of a significant size distribution. This effect is more apparent when examining H_C at $\alpha = 90°$, where a $\sim 11\%$ decrease from H_C at $\alpha = 0°$ is observed; while in the Ni$_{80}$Fe$_{20}$ nanowire arrays, this decrease ranged from 55% to 100%.

Figure 5.4 shows the coercive field as a functions of T$^{1/2}$ (for a symmetric energy landscape) and T$^{2/3}$ (for an asymmetric energy landscape)[96] with regimes marked. Below 100 K, the coercivity is linear with respect to T$^{2/3}$, indicating that the strong coupling of the trimerons causes an asymmetric energy landscape. This is consistent with a localized reversal mode caused by crystal defects and domain wall pinning.[97] Above 100 K, the $\alpha = 0°$ and $\alpha = 90°$ samples are linear with respect to T$^{1/2}$, indicating the recovery of a symmetric energy landscape. In this regime, classical reversal modes such as incoherent rotation and curling are favoured. For $\alpha = 90°$, the demagnetizing factor is minimized ($\mathcal{N}$ approaches 0), resulting in the critical diameter for curling, given by

$$d_c = 2q \left(\frac{2}{\mathcal{N}} \right)^{1/2} \frac{A^{1/2}}{M_S} \tag{5.1}$$

approaching infinity. Thus, we propose that reversal occurs via coherent rotation for $\alpha = 90°$, and curling for $\alpha = 0°$ above 150 K.

In contrast to the other orientations, the $\alpha = 45°$ system has two linear regimes
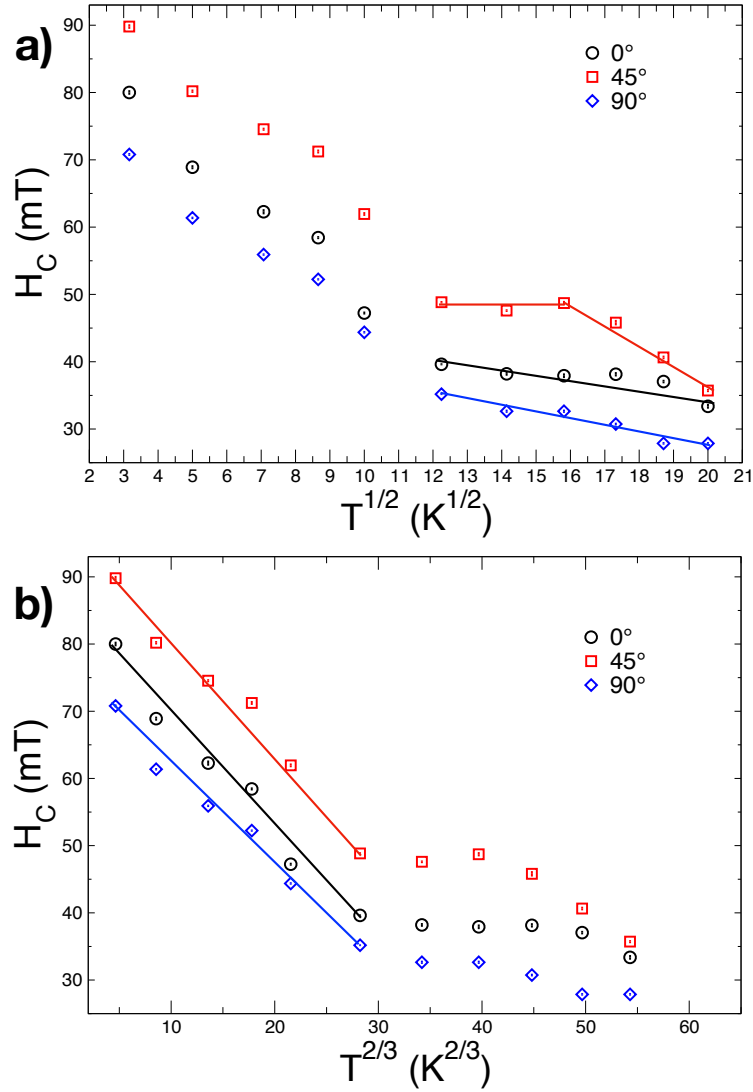
Figure 5.4: Coercive field of Fe_3O_4 nanorods with respect to a) $T^{1/2}$ and b) $T^{2/3}$ (bottom) for $\alpha = 0°$ (black circles), $\alpha = 45°$ (red squares), and $\alpha = 90°$ (blue diamonds). Linear regimes are indicates with lines.

above 150 K. We attribute the inflection point at 250 K to the structural transition between cubic and monoclinic states causing changes to both the anisotropy of the system and the magnetic easy axis. Above this temperature, H_C decreases, approaching H_C for $\alpha = 0°$. However, even at 400 K, the coercive field at $\alpha = 0°$ does not
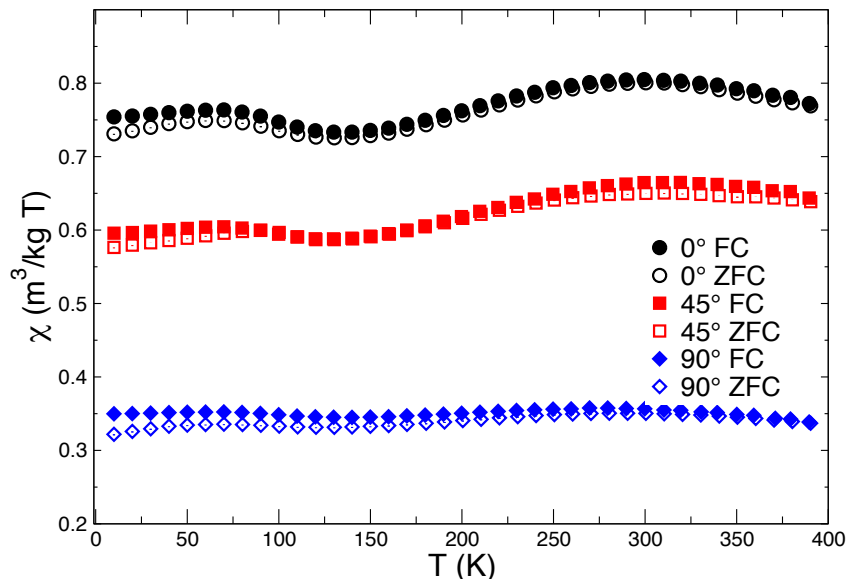
Figure 5.5: DC susceptibility (χ_{DC}) of Fe$_3$O$_4$ nanorods for $\alpha = 0°$ (black circles), $\alpha = 45°$ (red squares), and $\alpha = 90°$ (blue diamonds) in 5 mT. Zero-field cooled (ZFC) portion is indicated by open markers, while field cooled (FC) portion markers are closed.

exceed H_C at $\alpha = 45°$ as predicted for coherent rotation, indicating that some fraction of the sample still reverses via curling. We attribute this to the large size distribution within the Fe$_3$O$_4$ nanorods, since larger rods will continue to reverse via curling even when α is increased by the structural transition.[28]

To obtain further insights, the DC susceptibility (χ_{DC}) of all three alignments was measured using a 5 mT applied field under both zero-field cooled (ZFC) and field cooled (FC) conditions. These measurements are presented in Figure 5.5. Upon first inspection, the susceptibilities have a similar temperature dependence as M_R/M_S with the magnitude decreasing with increasing angle, and local minima at ∼130 K reflecting the impact of trimeron dissolution. The $\alpha = 45°$ sample and $\alpha = 90°$ samples have 81% and 45%, respectively, of the $\alpha = 0°$ χ_{DC}. Similar to the squareness

ratio, these results reflect the increase in the angle between the applied field and the magnetic easy axis causing change to the energy landscape. Further insights into the system are obtained from the differences between the FC and ZFC susceptibilities.

For magnetic nanoparticles, $\Delta\chi_{DC}$ is usually used to identify the blocking temperature, where the system becomes superparamagnetic.[21] However, for the Fe_3O_4 nanorods, this parameter provides insight into the effects of field cooling on the system. From Figure 5.6, there are features between 50 K and 120 K in both the $\alpha = 0°$ and $\alpha = 45°$ reflecting a change in the region where trimerons exist. However, we
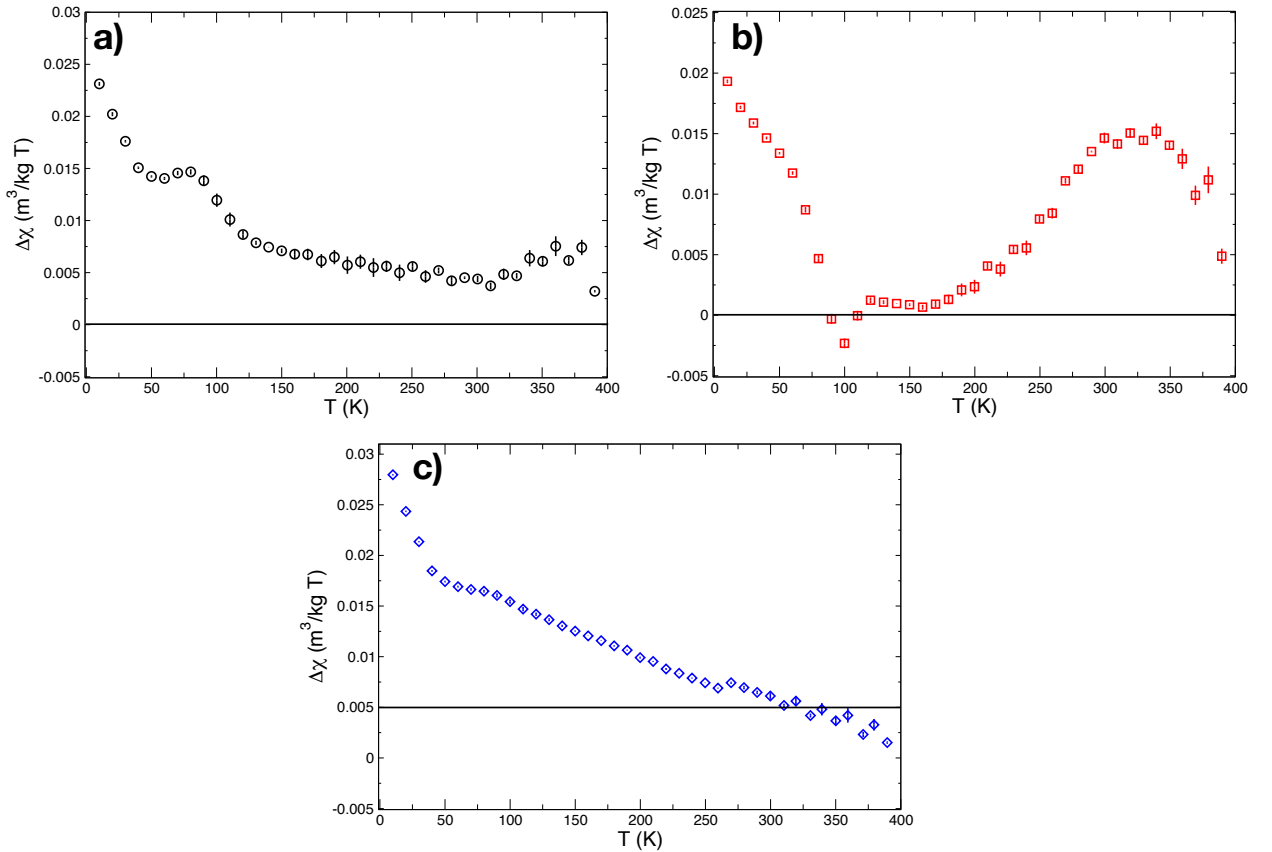
Figure 5.6: Difference between field cooled and zero-field cooled susceptibilities of a) $\alpha = 0°$, b) $\alpha = 45°$, and c) $\alpha = 90°$.

cannot attribute this solely to field cooling, because the structural transition observed between 225 K and 250 K upon warming, and 215 K upon cooling, revealed hysteresis in the system. Further experiments, including field cooled magnetometry and Mössbauer spectroscopy in an applied magnetic field, could be used to identify if the applied magnetic field induces a change in the coordination of trimerons or if the difference is caused by measuring on warming vs cooling cycles.

Between 150 K and 400 K $\Delta\chi_{DC}$ of $\alpha = 45°$ exhibits a local maximum. From the high coercive field, this orientation is associated with the largest energy barrier to reversal and is close to where the system transitions between curling and coherent rotation. It is possible that field cooling allows the system to reorient such the susceptibility of the FC portion is increased. Interestingly, features $\Delta\chi_{DC}$ are only significant in the orientations where curling is observed; the $\alpha = 90°$ $\Delta\chi_{DC}$ decreases monotonically with increasing temperature.

5.2   Summary

Examining the overall magnetism provides further insight into the effects of shape. The Fe$_3$O$_4$ nanorods reverse via curling for $\alpha = 0°$ and $\alpha = 45°$ above 150 K, while $\alpha = 0°$ reverses via coherent rotation. Below 150 K, all orientations of nanorods reverse in a localized reversal mode; we attribute this to the presence of trimerons. Implicit to this discussion, is the assumption of a fixed easy axis; however, the transition between monoclinic and cubic structures results causes the easy axis to shift. As a result, the assigned angles (α) of the majority of the sample will be slightly shifted below ~250 K.

Up to this point, all measurements had been done on samples cooled in zero magnetic field, however, the DC susceptibility shows different behaviours for $\alpha = 0°$ and $\alpha = 45°$ between zero-field cooling and field cooling measurements. Because this system contains transitions to both the structure and magnetism at different temperatures, further experiments are required to determine how field cooling affects these transitions.

Chapter 6

Fe_3O_4 nanorod hyperthermia

While examining the properties of the Fe_3O_4 nanorods as a function of temperature
and shape provides insights into the physics of their structure and magnetism, one
of the aims of this work is to evaluate their suitability for applications. In partic-
ular, anisotropic shaped particles have been proposed for their use in hyperthermia
treatments. For cancer treatments, the target temperature for malignant cell death is
41–46°C.[98][99] As a further constaint, Brezovich et al.[100] have determined that a
product of field (H) and frequency (f) below 4.85×10^8 A/m·s is required to prevent
excessive heating in patients. However, these nanorods are not suitable for in vivo
applications as their size increases the risk of obstructing blood vessels; thus we are
not limited by these constraints. In Chapter 3 we have shown that the heating re-
sponse of nanoparticles to an AC magnetic field leads to greater biofilm dissociation.
For this application, we aim to maximize the heating response, while minimizing both
the particle concentration and magnetic field.

To evaluate the heating response, suspensions of 0.5 mg/ml, 1.0 mg/ml, 1.5 mg/ml

and 2.0 mg/ml were tested using magnetic fields of 25 kA/m, 37.5 kA/m, and 50 kA/m. The acquired heating curves for the four concentrations are shown in Figure 6.1. The Ambrell Easyheat determines the AC frequency via impedance matching; because the variations in concentration do not add significant impedance to the system the frequency scales with applied field. As a result, the 25 kA/m magnetic field was applied at 197 kHz, while 37.5 kA/m and 50 kA/m both used 196 kHz. For all concentrations, the temperatures for magnetic fields 25 kA/m and 37.5 kA/m plateau at
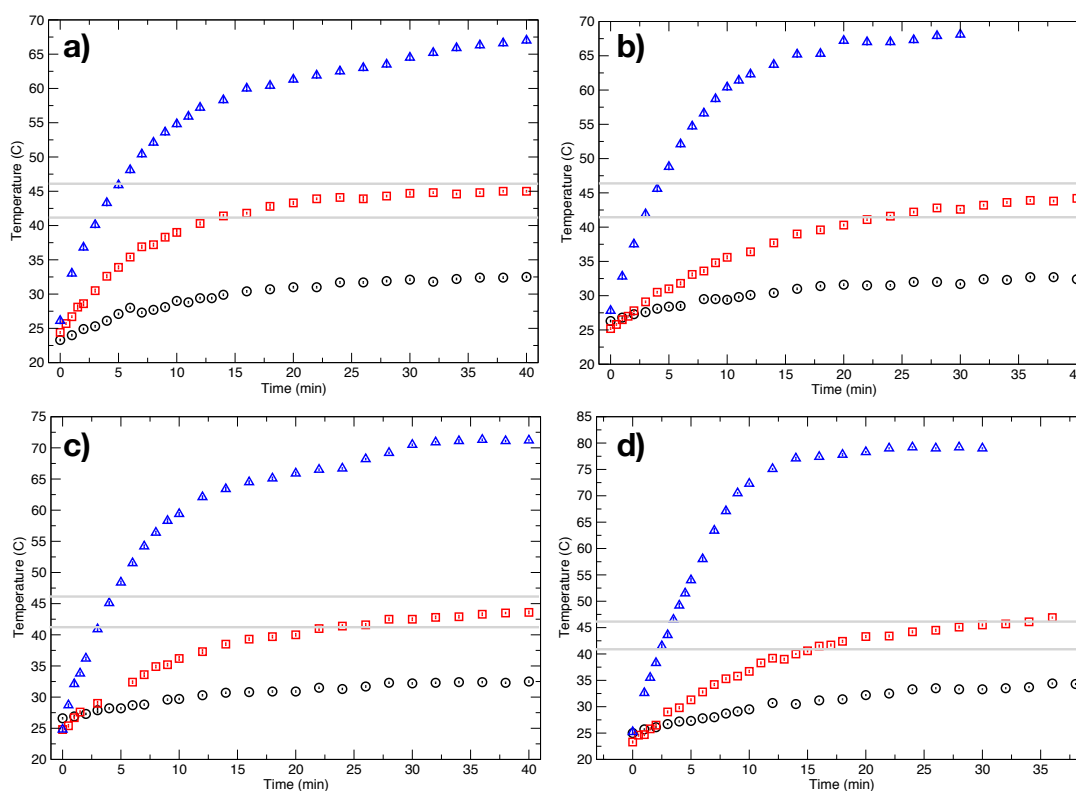
Figure 6.1: Heating curves of a) 0.5 mg/ml, b) 1.0 mg/ml, c) 1.5 mg/ml and d) 2.0 mg/ml Fe₃O₄ nanorods in water. Black circles are 25 kA/m, 197 kHz measurement, while red squares and blue triangles are 37.5 kA/m and 50 kA/m, respectively, both at 196 kHz. Grey lines indicate the targeted range for cell death (41– 46°C).

~33°C and ~45°C, respectively. In the 50 kA/m magnetic field, the maximum temperature increases with increasing concentrations with the temperature saturating between 66°C and 79°C.

To gain insights into the heating efficiency, the SLP of each measurement was calculated with respect to the Fe mass within the sample. As shown in Figure 6.2a), these values decrease with increasing concentration and increase with magnetic field, with a
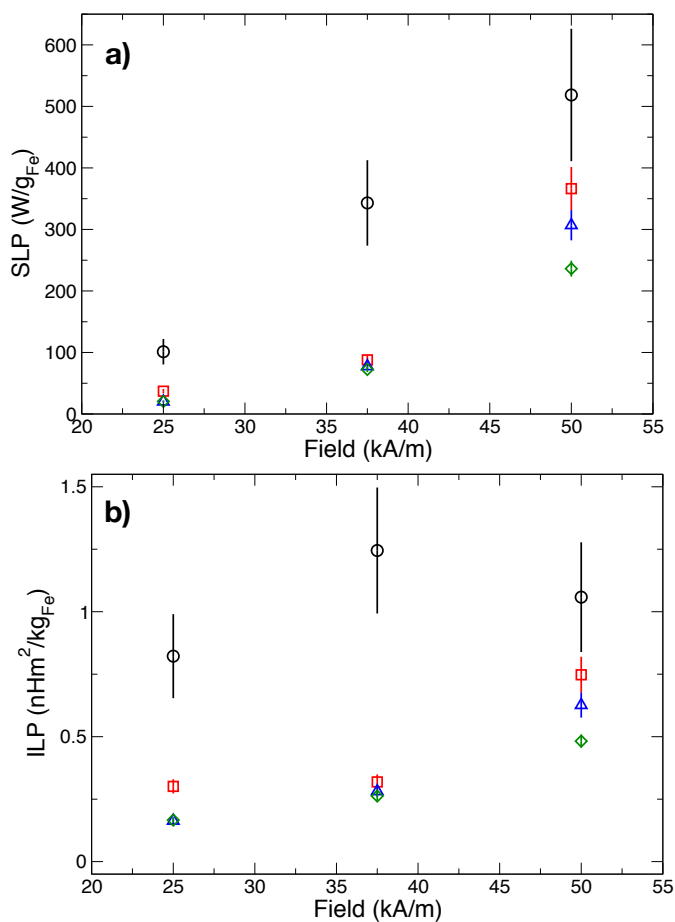
Figure 6.2: a) SLP and b) ILP of Fe_3O_4 nanorods in water normalized to the mass of Fe. Black circles are 0.5 mg/ml, red squares are 1.0 mg/ml, blue triangles are 1.5 mg/ml, and green diamonds are 2 mg/ml.

maximum value of 500±100 W/g$_{Fe}$. Due to the impact of the magnetic field and frequency on SLP, it is difficult to directly compare SLP results to literature values. As such, we have calculated the intrinsic loss power (ILP) given by ILP=SLP/(H^{2}f).[101] The ILP as a function of magnetic field is shown in Figure 6.2b).

While the ILP confirms the 0.5 mg/ml concentration as the most efficient, this representation is meant to remove the dependence of SLP on magnetic field. From Figure 6.2b), that is not true for the Fe$_3$O$_4$ nanorods, because the ILP was formulated assuming a single domain particle with coherent rotation. Nonetheless, the intrinsic loss power remains the most straightforward tool to compare literature values due to the large variations in the parameters used to test the heating response and thus the SLP values reported. The maximum ILP with respect to iron mass for our system is 1.2±0.3 nH·m^2/kg.

To put this into perspective, commercial hyperthermia samples have ILP values ranging from 0.15 to 3.12 nH·m^2/kg for concentrations of 5 mg/ml.[101] Of greater interest are the reported values for anisotropic nanoparticles. Iron oxide nanocubes (19±2 nm) by Guardia et al. have some of the highest measured SLP and ILP values at 2452 W/g and 5.6 nH·m^2/kg, respectively; however, the concentration of nanoparticles is not specified.[102] Since our nanorod data reveals a concentration dependence, this is a cause for concern because it is yet another factor the interferes with direct comparisons. To put this effect in perspective, Walter et al.[15] have have also shown that SLP decreases with increasing concentration of 16 nm Fe$_3$O$_4$ nanocubes. At 0.23 mg/ml the ILP was 1.1±0.2 nH·m^2/kg, while at 0.54 mg/ml, the ILP of this system was 0.38±0.05 nH·m^2/kg. Thus, while nanocubes have attracted significant

attention for their substantial SLP values, comparison of ILP values reveal nanorods as an equally exciting option for hyperthermia applications.

Chapter 7

Conclusions and Future Work

Iron oxide nanoparticles have been targeted for a variety of applications because they are highly modifiable, non-toxic to humans, and can be straightforward to synthesize. However, to optimize a system for a particular use, a full understanding of the underlying physics is required. Small changes to size and shape of nanoparticles can have significant effects on the behaviour of these systems. In our study of biofilm reduction, 11 nm spherical particles had an enhanced efficacy over 8 nm spherical particles. Because the improvements of larger nanoparticles can be attributed to differences in zeta potential and an enhanced hyperthermic response, anisotropic particles are an exciting option.

But switching to an anisotropic system has many consequences, due to the appearance of shape anisotropy and strain. In our study of magnetite (Fe_3O_4) nanorods, the appearance of uniaxial strain has significant effects on the Verwey transition. The strain is evidenced by the low temperature monoclinic phase distortion, with the lattice parameters indicating compression within the nanorods. From Mössbauer

spectroscopy, we are able to confirm the formation of trimerons; however, the fit results reveal a slightly different microstructure than bulk Fe_3O_4. In bulk magnetite, the Verwey transition occurs sharply at $\sim$120 K. This is in contrast to the nanorods, where a multi-step Verwey transition is observed, with trimerons dissociating at 150 K and the overall structural transition between 225 K and 250 K. Because the increased transition temperature is caused by uniaxial strain, these results give insight into how the Verwey temperature could be controlled.

Whilst the shape of the nanorods has been intrinsic to the observed transitions because the strain is caused by the shape, the shape of the particles explicitly affects the magnetic reversal. By examining the overall magnetic response for three orientations of nanoparticles, we observe curling above 150 K when the angle between the easy axis and magnetic field (α) is 0° and 45°, and coherent rotation for $\alpha = 90°$. Below 150 K (within the trimeron region), all orientations reverse via a localized reversal mode. Understanding the reversal mechanism is important, because the response to an applied magnetic field sets the foundation for magnetic hyperthermia.

The effect of curling was evident in the magnetic field dependence of the ILP of the Fe_3O_4 nanorods. ILP was formulated to remove the dependence on both magnetic field and frequency from SLP measurements to facilitate comparisons between different measurements; however, it was build upon the assumption of single domain particles with coherent rotation. Our measurements reveal that the formulation of ILP will require modification to account for incoherent reversal modes. Nonetheless, because the ILP for magnetite nanorods is comparable to that of iron oxide nanocubes, nanorods are a promising option for hyperthermia.

The logical next step for this work is to examine the efficacy of the Fe_3O_4 nanorods against MRSA biofilms. Because these nanorods are more difficult to synthesize in large quantities than the spherical nanoparticles, minimizing the iron oxide concentration is important. However, since there was minimal difference in the saturation temperature with concentration, a low particle concentration seems feasible. Additionally, because the mechanism behind the biofilm reduction appears to not be affected by the type of nanoparticles, this treatment has the potential to be recyclable as long the nanoparticles could be recovered and sanitized. Mössbauer spectroscopy will be necessary to monitor the effect of the sanitization on the nanoparticle composition, since traditional methods such as bleaching and autoclaving samples could affect the iron oxide phase. A slight change in composition would have significant effects on the magnetic response and thus heating efficiency, so it is essential that the system is unchanged.

While our intention is to examine other sizes and shapes of anisotropic nanoparticles, the field cooled susceptibility measurement suggests that the transitions within the Fe_3O_4 nanorods could be affected by an external magnetic field. Field cooled hysteresis loops and Mössbauer spectroscopy would provide further insight into the effect of field cooling on both the overall magnetic response and the microstructure. With these experiments, we hope to determine if the magnetic field affects the formation of trimerons, as well as any effect on the temperature dependence of the Verwey transition. Additionally, a full quantitative analysis of the low temperature XRD patterns will be performed to track the evolution of the lattice as a function of temperature for both cooling and warming cycles.

Once these nanorods are fully characterized, we will focus on other systems, particularly smaller nanorods and nanodisks. While we have shown in this work that uniaxial compression increases the Verwey temperature in nanorods, a new discovery, future work will be focused on determining the relationship between uniaxial strain and the Verwey transition. The low temperature monoclinic structure provides an indicator for the degree of strain within the system, while Mössbauer spectroscopy and XAS/XMCD provide information about the local coordination of trimerons. Low temperature XRD will also be used to track the structural evolution of the system. Overall, the aim of this study would be to determine how uniaxial strain could be used to increase the Verwey temperature, so that applications could take advantage of the unique properties resulting from the Verwey transition. Concurrently, hyperthermia studies could be performed to evaluate the different shapes' suitability for biomedical applications.

Bibliography

[1] Xavier Batlle and Amílcar Labarta. Finite-size effects in fine particles: magnetic and transport properties. *Journal of Physics D: Applied Physics*, 35:R15, 2002.

[2] Andreas Moser, Kentaro Takano, David T Margulies, Manfred Albrecht, Yoshiaki Sonobe, Yoshihiro Ikeda, Shouheng Sun, and Eric E Fullerton. Magnetic recording: advancing into the future. *Journal of Physics D: Applied Physics*, 35(19):R157, 2002.

[3] L-S Zhong, J-S Hu, H-P Liang, A-M Cao, W-G Song, and L-J Wan. Self-assembled 3D flowerlike iron oxide nanostructures and their application in water treatment. *Advanced Materials*, 18(18):2426–2431, 2006.

[4] Quentin A Pankhurst, J Connolly, SK Jones, and J Dobson. Applications of magnetic nanoparticles in biomedicine. *Journal of physics D: Applied physics*, 36(13):R167, 2003.

[5] Radek Zboril, Miroslav Mashlan, and Dimitris Petridis. Iron (III) oxides from thermal processes synthesis, structural and magnetic properties, Mössbauer spectroscopy characterization, and applications. *Chemistry of Materials*, 14(3):969–982, 2002.

[6] Shin-ichi Ohkoshi and Hiroko Tokoro. Hard magnetic ferrite: ε-Fe_2O_3. *Bulletin of the Chemical Society of Japan*, 86(8):897–907, 2013.

[7] Changzheng Wu, Ping Yin, Xi Zhu, Chuanzi OuYang, and Yi Xie. Synthesis of hematite (α-Fe_2O_3) nanorods: diameter-size and shape effects on their applications in magnetism, lithium ion battery, and gas sensors. *The Journal of Physical Chemistry B*, 110(36):17806–17812, 2006.

[8] Kevin Sivula, Florian Le Formal, and Michael Grätzel. Solar water splitting: progress using hematite (α-Fe_2O_3) photoelectrodes. *ChemSusChem*, 4(4):432–449, 2011.

[9] Ret al Weissleder, David D Stark, Barry L Engelstad, Bruce R Bacon, Carolyn C Compton, David L White, Paula Jacobs, and Jerome Lewis. Superparamagnetic iron oxide: pharmacokinetics and toxicity. *American Journal of Roentgenology*, 152(1):167–173, 1989.

[10] Manuel Arruebo, Rodrigo Fernández-Pacheco, M Ricardo Ibarra, and Jesús Santamaría. Magnetic nanoparticles for drug delivery. *Nano today*, 2(3):22–32, 2007.

[11] LX Tiefenauer, A Tschirky, G Kühne, and RY Andres. In vivo evaluation of magnetite nanoparticles for use as a tumor contrast agent in MRI. *Magnetic resonance imaging*, 14(4):391–402, 1996.

[12] Rudolf Hergt, Wilfried Andra, Carl G d'Ambly, Ingrid Hilger, Werner A Kaiser,

Uwe Richter, and H-G Schmidt. Physical limits of hyperthermia using magnetite fine particles. *IEEE Transactions on Magnetics*, 34(5):3745–3754, 1998.

[13] Sang-Jae Park, Seungsoo Kim, Suyoun Lee, Zheong G Khim, Kookrin Char, and Taeghwan Hyeon. Synthesis and magnetic studies of uniform iron nanorods and nanospheres. *Journal of the American Chemical Society*, 122(35):8581–8582, 2000.

[14] Wei-Syuan Lin, Hong-Ming Lin, Hsiang-Hsin Chen, Yeu-Kuang Hwu, and Yuh-Jing Chiou. Shape effects of iron nanowires on hyperthermia treatment. *Journal of Nanomaterials*, 2013:9, 2013.

[15] Aurélie Walter, Claire Billotey, Antonio Garofalo, Corinne Ulhaq-Bouillet, Christophe Lefèvre, Jacqueline Taleb, Sophie Laurent, Luce Vander Elst, Robert N Muller, Lénaïc Lartigue, et al. Mastering the shape and composition of dendronized iron oxide nanoparticles to tailor magnetic resonance imaging and hyperthermia. *Chemistry of Materials*, 26(18):5252–5264, 2014.

[16] John B Goodenough. Theory of the role of covalence in the perovskite-type manganites [La,M(II)]MnO$_3$. *Physical Review*, 100(2):564, 1955.

[17] Junjiro Kanamori. Superexchange interaction and symmetry properties of electron orbitals. *Journal of Physics and Chemistry of Solids*, 10(2-3):87–98, 1959.

[18] Joachim Stöhr and Hans Christoph Siegmann. *Magnetism: from fundamentals to nanoscale dynamics*, volume 152. Springer Science & Business Media, 2007.

[19] J. M. D. Coey. *Magnetism and magnetic materials.* Cambridge University Press, Cambridge, 2010.

[20] Jean-Louis Dormann, Dino Fiorani, and Elisabeth Tronc. Magnetic relaxation in fine-particle systems. *Advances in Chemical Physics, Volume 98*, pages 283–494.

[21] Amikam Aharoni. *Introduction to the Theory of Ferromagnetism*, volume 109. Clarendon Press, 2000.

[22] Robert F Butler and Subir K Banerjee. Theoretical single-domain grain size range in magnetite and titanomagnetite. *Journal of Geophysical Research*, 80(29):4049–4058, 1975.

[23] EC Stoner and EP Wohlfarth. A mechanism of magnetic hysteresis in heterogeneous alloys. *IEEE Transactions on Magnetics*, 27(4):3475–3518, 1991.

[24] Alberto P Guimarães and Alberto Passos Guimaraes. *Principles of nanomagnetism*, volume 7. Springer, 2009.

[25] Robert C O'Handley. *Modern magnetic materials: principles and applications.* Wiley, 2000.

[26] EH Frei, S Shtrikman, and D Treves. Critical size and nucleation field of ideal ferromagnetic particles. *Physical Review*, 106(3):446, 1957.

[27] S Shtrikman and D Treves. The coercive force and rotational hysteresis of elongated ferromagnetic particles. *J. phys. radium*, 20(2-3):286–289, 1959.

[28] Amikam Aharoni. Angular dependence of nucleation by curling in a prolate spheroid. *Journal of applied physics*, 82(3):1281–1287, 1997.

[29] Walter Kündig and R Steven Hargrove. Electron hopping in magnetite. *Solid State Communications*, 7(1):223–227, 1969.

[30] ME Fleet. The structure of magnetite. *Acta Crystallographica Section B: Structural Crystallography and Crystal Chemistry*, 37(4):917–920, 1981.

[31] Biljana D Stojanovic. *Magnetic, Ferroelectric, and Multiferroic Metal Oxides*, volume 1. Elsevier, 2018.

[32] EJW Verwey. Electronic conduction of magnetite (Fe_3O_4) and its transition point at low temperatures. *Nature*, 144(3642):327, 1939.

[33] M Iizumi, TF Koetzle, G Shirane, S Chikazumi, M Matsui, and S Todo. Structure of magnetite (Fe_3O_4) below the Verwey transition temperature. *Acta Crystallographica Section B: Structural Crystallography and Crystal Chemistry*, 38(8):2121–2133, 1982.

[34] Javier Blasco, Joaquín García, and Gloria Subías. Structural transformation in magnetite below the Verwey transition. *Physical Review B*, 83(10):104105, 2011.

[35] EJ Verwey, PW Haayman, and FC Romeijn. Physical properties and cation arrangement of oxides with spinel structures II. Electronic conductivity. *The Journal of Chemical Physics*, 15(4):181–187, 1947.

[36] Friedrich Walz. The Verwey transition–a topical review. *Journal of Physics: Condensed Matter*, 14(12):R285, 2002.

[37] Joaquín García and Gloria Subías. The Verwey transition: a new perspective. *Journal of Physics: Condensed Matter*, 16(7):R145, 2004.

[38] Horng-Tay Jeng, GY Guo, and DJ Huang. Charge-orbital ordering in low-temperature structures of magnetite: GGA+ U investigations. *Physical Review B*, 74(19):195115, 2006.

[39] Mark S Senn, Jon P Wright, and J Paul Attfield. Charge order and three-site distortions in the Verwey structure of magnetite. *Nature*, 481(7380):173, 2012.

[40] Mark S Senn, Ingo Loa, Jon P Wright, and J Paul Attfield. Electronic orders in the Verwey structure of magnetite. *Physical Review B*, 85(12):125119, 2012.

[41] R Řezníček, V Chlan, H Štěpánková, and P Novák. Hyperfine field and electronic structure of magnetite below the Verwey transition. *Physical Review B*, 91(12):125134, 2015.

[42] S De Jong, R Kukreja, Christoph Trabant, N Pontius, CF Chang, T Kachel, M Beye, F Sorgenfrei, CH Back, B Bräuer, et al. Speed limit of the insulator–metal transition in magnetite. *Nature materials*, 12(10):882, 2013.

[43] G Kh Rozenberg, MP Pasternak, WM Xu, Y Amiel, M Hanfland, M Amboage, RD Taylor, and R Jeanloz. Origin of the Verwey transition in magnetite. *Physical review letters*, 96(4):045705, 2006.

[44] MP Pasternak, WM Xu, G Kh Rozenberg, RD Taylor, and R Jeanloz. Pressure-induced coordination crossover in magnetite, a high pressure Mössbauer study. *Journal of Physics and Chemistry of Solids*, 65(8-9):1531–1535, 2004.

[45] Xionghua Liu, Chun-Fu Chang, Aurora Diana Rata, Alexander Christoph Komarek, and Liu Hao Tjeng. Fe_3O_4 thin films: controlling and manipulating an elusive quantum material. *npj Quantum Materials*, 1:16027, 2016.

[46] XH Liu, W Liu, and ZD Zhang. Evolution of magnetic properties in the vicinity of the Verwey transition in Fe_3O_4 thin films. *Physical Review B*, 96(9):094405, 2017.

[47] Xiang Liu, Li Yin, and Wenbo Mi. Biaxial strain effect induced electronic structure alternation and trimeron recombination in Fe_3O_4. *Scientific reports*, 7:43403, 2017.

[48] Yasuo Nagasawa, Masashi Kosaka, Susumu Katano, Nobuo Môri, Sakae Todo, and Yoshiya Uwatoko. Effect of uniaxial strain on Verwey transition in magnetite. *Journal of the Physical Society of Japan*, 76(Suppl. A):110–111, 2007.

[49] A.L. Patterson. The Scherrer formula for x-ray particle size determination. *Physical Review*, 978:11536–11546, 1939.

[50] Vitalij Pecharsky and Peter Zavalij. *Fundamentals of powder diffraction and structural characterization of materials*. Springer Science & Business Media, 2008.

[51] Juan Rodríquez-Carvajal and T Roisnel. Line broadening analysis using Full-
Prof: determination of microstructural properties. In *Materials Science Forum*,
volume 443, pages 123–126. Trans Tech Publ, 2004.

[52] Brian H Toby and Robert B Von Dreele. GSAS-II: the genesis of a modern
open-source all purpose crystallography software package. *Journal of Applied
Crystallography*, 46(2):544–549, 2013.

[53] Bruce J Berne and Robert Pecora. *Dynamic light scattering: with applications
to chemistry, biology, and physics.* Courier Corporation, 2000.

[54] Tharwat F Tadros. *Dispersion of powders in liquids and stabilization of sus-
pensions.* John Wiley & Sons, 2012.

[55] Rudolf L Mössbauer. Kernresonanzfluoreszenz von gammastrahlung in Ir^{191}.
Zeitschrift für Physik, 151(2):124–143, 1958.

[56] N.N. Greenwood and T.C. Gibb. *Mossbauer Spectroscopy.* John Wiley & Sons,
Incorporated, 1971.

[57] RM Housley, U Gonser, and RW Grant. Mössbauer determination of the debye-
waller factor in single-crystal absorbers. *Physical Review Letters*, 20(23):1279,
1968.

[58] M Darby Dyar, David G Agresti, Martha W Schaefer, Christopher A Grant, and
Elizabeth C Sklute. Mössbauer spectroscopy of earth and planetary materials.
Annu. Rev. Earth Planet. Sci., 34:83–125, 2006.

[59] Philipp Gütlich, Eckhard Bill, and Alfred X Trautwein. *Mössbauer spectroscopy and transition metal chemistry: fundamentals and applications.* Springer Science & Business Media, 2010.

[60] Caroline A Schneider, Wayne S Rasband, and Kevin W Eliceiri. NIH Image to ImageJ: 25 years of image analysis. *Nature methods*, 9(7):671, 2012.

[61] Mike McElfresh. Fundamentals of magnetism and magnetic measurement, 1994.

[62] Eric Beaurepaire, Fabrice Scheurer, Gérard Krill, and Jean-Paul Kappler. *Magnetism and synchrotron radiation*, volume 34. Springer, 2001.

[63] CT Chen, YU Idzerda, H-J Lin, NV Smith, G Meigs, E Chaban, GH Ho, E Pellegrin, and F Sette. Experimental confirmation of the x-ray magnetic circular dichroism sum rules for iron and cobalt. *Physical review letters*, 75(1):152, 1995.

[64] Marius Retegan. mretegan/crispy: v0.5.0, March 2018.

[65] G Vallejo-Fernandez, O Whear, AG Roca, S Hussain, J Timmis, V Patel, and K O'Grady. Mechanisms of hyperthermia in magnetic nanoparticles. *Journal of Physics D: Applied Physics*, 46(31):312001, 2013.

[66] World Health Organization. Antimicrobial resistance: global report on surveillance 2014, 2014.

[67] Hans-Curt Flemming and Jost Wingender. The biofilm matrix. *Nature Reviews Microbiology*, 8(9):623, 2010.

[68] JC Nickel, I Ruseska, JB Wright, and JW Costerton. Tobramycin resistance of Pseudomonas aeruginosa cells growing as a biofilm on urinary catheter material. *Antimicrobial agents and chemotherapy*, 27(4):619–624, 1985.

[69] Sophie Laurent, Delphine Forge, Marc Port, Alain Roch, Caroline Robic, Luce Vander Elst, and Robert N Muller. Magnetic iron oxide nanoparticles: synthesis, stabilization, vectorization, physicochemical characterizations, and biological applications. *Chemical reviews*, 108(6):2064–2110, 2008.

[70] Hakim Rahma, Rachel Nickel, Elizabeth Skoropata, Yaroslav Wroczynskyj, Christopher Rutley, Palash K Manna, Ching Hung Hsiao, Hao Ouyang, Johan van Lierop, and Song Liu. Quaternized N-chloramine coated magnetic nanoparticles: a trifecta of superior antibacterial activity, minimal residual toxicity and rapid site removal. *RSC Advances*, 6(70):65837–65846, 2016.

[71] Xuejing Chen, Jianguo Jiang, Feng Yan, Sicong Tian, and Kaimin Li. A novel low temperature vapor phase hydrolysis method for the production of nano-structured silica materials using silicon tetrachloride. *RSC Advances*, 4(17):8703–8710, 2014.

[72] Catherine McCammon. Mössbauer spectroscopy of minerals. *Mineral physics & crystallography: A handbook of physical constants*, pages 332–347, 1995.

[73] Jr. Chase, M.W. NIST-JANAF themochemical tables, fourth edition, 1998.

[74] Katarzyna Niemirowicz, Ewelina Piktel, Agnieszka Z Wilczewska, Karolina H Markiewicz, Bonita Durnaś, Marzena Watek, Irena Puszkarz, Marta

Wróblewska, Wiesława Niklińska, Paul B Savage, et al. Core–shell magnetic nanoparticles display synergistic antibacterial effects against Pseudomonas aeruginosa and Staphylococcus aureus when combined with cathelicidin ll-37 or selected ceragenins. *International journal of nanomedicine*, 11:5443, 2016.

[75] Thuy-Khanh Nguyen, Hien TT Duong, Ramona Selvanayagam, Cyrille Boyer, and Nicolas Barraud. Iron oxide nanoparticle-mediated hyperthermia stimulates dispersal in bacterial biofilms and enhances antibiotic efficacy. *Scientific reports*, 5:18385, 2015.

[76] Françoise Van Bambeke, Marie-Paule Mingeot-Leclercq, Marc J Struelens, and Paul M Tulkens. The bacterial envelope as a target for novel anti-MRSA antibiotics. *Trends in pharmacological sciences*, 29(3):124–134, 2008.

[77] Matthias Gross, Sarah E Cramton, Friedrich Götz, and Andreas Peschel. Key role of teichoic acid net charge in Staphylococcus aureus colonization of artificial surfaces. *Infection and immunity*, 69(5):3423–3426, 2001.

[78] Gang Liu, Jinhao Gao, Hua Ai, and Xiaoyuan Chen. Applications and potential toxicity of magnetic iron oxide nanoparticles. *Small*, 9(9-10):1533–1545, 2013.

[79] Mohd Imran Khan, Akbar Mohammad, Govil Patil, SAH Naqvi, LKS Chauhan, and Iqbal Ahmad. Induction of ROS, mitochondrial damage and autophagy in lung epithelial cancer cells by iron oxide nanoparticles. *Biomaterials*, 33(5):1477–1488, 2012.

[80] Ronald E Rosensweig. Heating magnetic fluid with alternating magnetic field. *Journal of magnetism and magnetic materials*, 252:370–374, 2002.

[81] H Khurshid, J Alonso, Z Nemati, MH Phan, P Mukherjee, ML Fdez-Gubieda, JM Barandiarán, and H Srikanth. Anisotropy effects in magnetic hyperthermia: A comparison between spherical and cubic exchange-coupled FeO/Fe_3O_4 nanoparticles. *Journal of Applied Physics*, 117(17):17A337, 2015.

[82] J Alonso, H Khurshid, V Sankar, Z Nemati, MH Phan, E Garayo, JA Garcia, and H Srikanth. FeCo nanowires with enhanced heating powers and controllable dimensions for magnetic hyperthermia. *Journal of Applied Physics*, 117(17):17D113, 2015.

[83] GF Goya, TS Berquo, FC Fonseca, and MP Morales. Static and dynamic magnetic properties of spherical magnetite nanoparticles. *Journal of Applied Physics*, 94(5):3520–3528, 2003.

[84] Zhihui Xu, Jianru Liang, and Lixiang Zhou. Template-free hydrothermal synthesis of β-FeOOH nanorods and their catalytic activity in the degradation of methyl orange by a photo-fenton-like process. *Open Journal of Inorganic Non-Metallic Materials*, 3:58–65, 2013.

[85] AR Muxworthy and W Williams. Micromagnetic models of pseudo-single domain grains of magnetite near the Verwey transition. *Journal of Geophysical Research: Solid Earth*, 104(B12):29203–29217, 1999.

[86] EJW Verwey and PW Haayman. Electronic conductivity and transition point of magnetite (Fe$_3$O$_4$). *Physica*, 8(9):979–987, 1941.

[87] TJ Daou, G Pourroy, S Bégin-Colin, JM Greneche, C Ulhaq-Bouillet, P Legaré, P Bernhardt, C Leuvrey, and G Rogez. Hydrothermal synthesis of monodisperse magnetite nanoparticles. *Chemistry of Materials*, 18(18):4399–4404, 2006.

[88] Mark S Senn, Jon P Wright, James Cumby, and J Paul Attfield. Charge localization in the Verwey structure of magnetite. *Physical Review B*, 92(2):024104, 2015.

[89] JP Crocombette, M Pollak, F Jollet, N Thromat, and M Gautier-Soyer. X-ray-absorption spectroscopy at the Fe l$_{2,3}$ threshold in iron oxides. *Physical Review B*, 52(5):3143, 1995.

[90] Feng Lin, Dennis Nordlund, Taijun Pan, Isaac M Markus, Tsu-Chien Weng, Huolin L Xin, and Marca M Doeff. Influence of synthesis conditions on the surface passivation and electrochemical behavior of layered cathode materials. *Journal of Materials Chemistry A*, 2(46):19833–19840, 2014.

[91] ZY Wu, S Gota, F Jollet, M Pollak, M Gautier-Soyer, and CR Natoli. Characterization of iron oxides by x-ray absorption at the oxygen K-edge using a full multiple-scattering approach. *Physical Review B*, 55(4):2570, 1997.

[92] I Leonov, AN Yaresko, VN Antonov, and VI Anisimov. Electronic structure of charge-ordered Fe$_3$O$_4$ from calculated optical, magneto-optical Kerr effect, and O K-edge x-ray absorption spectra. *Physical Review B*, 74(16):165117, 2006.

[93] PM Paulus, F Luis, M Kröll, G Schmid, and LJ De Jongh. Low-temperature study of the magnetization reversal and magnetic anisotropy of Fe, Ni, and Co nanowires. *Journal of Magnetism and Magnetic Materials*, 224(2):180–196, 2001.

[94] S Goolaup, N Singh, AO Adeyeye, V Ng, and MBA Jalil. Transition from coherent rotation to curling mode reversal process in ferromagnetic nanowires. *The European Physical Journal B-Condensed Matter and Complex Systems*, 44(2):259–264, 2005.

[95] GC Han, BY Zong, P Luo, and YH Wu. Angular dependence of the coercivity and remanence of ferromagnetic nanowire arrays. *Journal of Applied Physics*, 93(11):9202–9207, 2003.

[96] RH Victora. Predicted time dependence of the switching field for magnetic materials. *Physical review letters*, 63(4):457, 1989.

[97] R Skomski, H Zeng, and DJ Sellmyer. Incoherent magnetization reversal in nanowires. *Journal of magnetism and magnetic materials*, 249(1-2):175–180, 2002.

[98] C Christophi, A Winkworth, V Muralihdaran, and P Evans. The treatment of malignancy by hyperthermia. *Surgical oncology*, 7(1-2):83–90, 1998.

[99] BV Harmon, YS Takano, CM Winterford, and GC Gobe. The role of apoptosis in the response of cells and tumours to mild hyperthermia. *International journal of radiation biology*, 59(2):489–501, 1991.

[100] Ivan A Brezovich. Low frequency hyperthermia: capacitive and ferromagnetic thermoseed methods. *Medical physics monograph*, 16:82–111, 1988.

[101] Mathew Kallumadil, Masaru Tada, Takashi Nakagawa, Masanori Abe, Paul Southern, and Quentin A Pankhurst. Suitability of commercial colloids for magnetic hyperthermia. *Journal of Magnetism and Magnetic Materials*, 321(10):1509–1513, 2009.

[102] Pablo Guardia, Riccardo Di Corato, Lenaic Lartigue, Claire Wilhelm, Ana Espinosa, Mar Garcia-Hernandez, Florence Gazeau, Liberato Manna, and Teresa Pellegrino. Water-soluble iron oxide nanocubes with high values of specific absorption rate for cancer cell hyperthermia treatment. *ACS nano*, 6(4):3080–3091, 2012.